Research Square

Preprints are preliminary reports that have not undergone peer review.
They should not be considered conclusive, used to inform clinical practice,
or referenced by the media as validated information.

Asymmetric vibration pattern enables ultrafast locomotion of an insect-scale amphibious microrobot

Liu Zhiwei

liuzhiwei1991@buaa.edu.cn

Beihang University https://orcid.org/0000-0002-7287-7333

Wencheng Zhan

Beihang University https://orcid.org/0000-0003-2604-9163

Xiaoxi Li

Beihang University

Delan Huang

Beihang University

Jia Hu

Beihang University

Xian Yu

Beihang University

Lizhao Wei

Beihang University

Jiaming Leng

Beihang University https://orcid.org/0000-0002-1824-2417

Heming Xu

AECC Commercial Aircraft Engine Co., LTD

Chunxiao Li

AECC Shenyang Liming Aero-Engine CO.,LTD.

Pei Cai

AECC Commercial Aircraft Engine Co.,LTD.

Xiaojun Yan

Beihang University https://orcid.org/0000-0002-6151-7279

Article

Keywords:

Posted Date: October 26th, 2026

DOI: https://doi.org/10.21203/rs.3.rs-11294123/v1

License: This work is licensed under a Creative Commons Attribution 4.0 International License.
Read Full License

Additional Declarations: There is **NO** Competing Interest.

Asymmetric vibration pattern enables ultrafast locomotion of an insect-scale amphibious microrobot

Authors

Wencheng Zhan[1]†, Xiaoxi Li[1]†, Zhiwei Liu[1,2,3,4 *], Delan Huang[1], Jia Hu[1], Xian Yu[1], Lizhao Wei[1], Jiaming Leng[5], Heming Xu[6], Chunxiao Li[6], Pei Cai[6], Xiaojun Yan[1,2,3,4 *]

†: These authors contributed equally to this work

*Corresponding authors:

Zhiwei Liu (liuzhiwei1991@buaa.edu.cn), Xiaojun Yan (yanxiaojun@buaa.edu.cn)

Affiliations

[1]School of Energy and Power Engineering, Beihang University, Beijing, China

[2]National Key Laboratory of Multi-perch Vehicle Driving Systems, Beijing, China

[3]Collaborative Innovation Center of Advanced Aero-Engine, Beijing, China

[4]Beijing Key Laboratory of Aero-Engine Structure and Strength, Beijing, China

[5]School of Automation and Electrical Engineering, BeiHang University, Beijing, China

[6]Aero Engine Corporation of China, Beijing, China

Abstract: Agile amphibious locomotion typically requires the implementation of distinct high-speed locomotion patterns across disparate environments, posing formidable challenges for insect-scale microrobots due to size limitation (body length less than 5 cm). In this study, we present an untethered and controlled amphibious microrobot measuring only 2.1 cm in length and weighing 1.69 g, capable of ultrafast locomotion on land and water surface. The microrobot utilizes a single set of actuators to generate an asymmetric vibration pattern for both terrestrial and aquatic locomotion. This pattern exploits resonance of the microrobot to achieve high agility while requiring only a structurally simple actuation mechanism. With onboard power and control units, the microrobot exhibits a maximum terrestrial speed of 32.5 cm/s (15.5 body lengths per second,

BL/s), and a maximum aquatic speed of 11.3 cm/s (5.4 BL/s). Besides, the microrobot also demonstrates wireless controlled obstacle avoidance, and ultrafast turns with a maximum turning speed of 760°/s on the ground and 450°/s on the water surface. Employing bipedal alternating vibrations of two actuation mechanisms, the microrobot can realize untethered transitions between ground and water surface via a slope. These results establish this microrobot as the smallest and fastest amphibious microrobot reported to date capable of untethered and controlled locomotion across both terrestrial and aquatic environments, including the transitional region.

Introduction

Several insects, such as water striders[1,2] and whirligig beetles[3-5], achieve high-speed linear locomotion and rapid turns in both terrestrial and aquatic environments utilizing the same set of legs. These impressive capabilities have motivated researchers to develop insect-scale amphibious robots (body length less than 5 cm) that can achieve high-speed, untethered, and controlled locomotion[6-9]. To achieve high agility in both terrestrial and aquatic environments, the conventional scheme utilizes separate actuators and actuation mechanisms to implement motion patterns suitable for terrestrial and aquatic locomotion, respectively. Based on this scheme, a variety of large-scale untethered amphibious robots have been proposed[10-12], with actuation mechanisms including limb movements with body undulations[12,13], claws with swimmerets[14,15], slapping and stroking of legs[16], dual swing legs with antibias wheels[17], flexible legs with adaptive shapes[18-21], and vectored water jet thrusters with legs[22-24]. Despite its satisfactory performance, such a scheme becomes impractical at the insect scale because it relies on multiple actuators and complex onboard power electronics that are difficult to miniaturize[25].

To reconcile miniaturization with agility, insect-scale amphibious microrobots tend to employ a single set of actuators to drive both terrestrial and aquatic actuation mechanisms[26,27]. However, the substantial differences between terrestrial and aquatic environments make it difficult for motion patterns based on a single set of actuators to achieve high-speed locomotion in both environments simultaneously. For example,

the HAMR microrobot employs one set of piezoelectric actuators to drive a crawling leg integrated with two flaps, generating an alternating tripod pattern for terrestrial and aquatic locomotion[27]. This pattern enables insect-like terrestrial locomotion, but in water, the low swing frequency of the flaps limits its speed. With a body length of 4.0 cm, HAMR achieves a terrestrial speed of 1.75 BL/s and an aquatic speed of 0.7 BL/s connected with an external power source[27]. Moreover, another microrobot, Leglessbot, utilizes an inertial driving pattern, in which a voice coil motor drives the body shell and fin arrays to produce propulsion force on the ground and water surface respectively[28]. Similarly, the pattern enables forward jumping on rough ground via the body shell, but the small-amplitude actuation of fin arrays results in low speed on the water surface[28]. With onboard power source and electronics, Leglessbot reaches 1.4 BL/s on land and 0.6 BL/s on water. Consequently, although substantial efforts have been devoted, no reported microrobot to date has achieved high-speed, untethered, and controlled amphibious locomotion simultaneously. To achieve high agility at the insect scale, it is necessary to develop motion patterns that not only rely on a single set of actuators but also simultaneously support high-speed terrestrial and aquatic locomotion.

In this work, we present an insect-scale amphibious microrobot (2.1 cm, 1.69 g), capable of ultrafast, untethered and controlled locomotion on both ground and water surface, as well as water–land transitions. An asymmetric vibration pattern is proposed that exploits resonance to generate substantial propulsion forces on the ground or water surface and achieves insect-like agile locomotion. Furthermore, the motion pattern is enabled by simple actuation mechanisms that allow amphibious locomotion to share the same set of actuators, such as the mechanism in this work that combines a running leg and a swimming paddle. Consequently, this pattern not only allows shared actuators for miniaturization but also accommodates rapid locomotion on both land and water surface, thereby eliminating the need for a trade-off between size and agility. The crucial factors influencing the aquatic and terrestrial speed are investigated by modeling and experiments for optimization of the amphibious locomotion performance of the microrobot. An onboard power and control circuit is also designed to demonstrate untethered and controlled amphibious locomotion. Under wireless

commands, the untethered microrobot exhibits a maximum aquatic speed of 5.4 BL/s and a maximum terrestrial speed of 15.5 BL/s. Furthermore, obstacles avoidance and transitions between the water surface and the ground have also been demonstrated by the untethered microrobot.

Results

Microrobot design and asymmetric vibration pattern

Bioinspired microrobots emerge as promising tools for exploration and rescue in complex terrains and confined spaces[7,29,30], which is further enhanced when amphibious locomotion is integrated into insect-scale platforms[27,31,32]. Fig. 1a shows the schematic diagram of an amphibious microrobot conducting simulated exploration tasks across terrestrial and aquatic terrains. Fig. 1b illustrates the presented amphibious microrobot (2.1 cm, 1.69 g) integrated with an onboard battery and a power and control circuit, floating on the water surface. It consists of a pair of linear electromagnetic actuators, a pair of actuation mechanisms integrating with a running leg and a swimming paddle, rear supporting legs, floating pads and a buoyancy tank (Fig. 1c). To realize miniaturization, the microrobot is designed to generate propulsions for amphibious locomotion by driving the integrated actuation mechanism via the same set of actuators. Directional control in both environments is enabled by two independent electromagnetic actuators arranged symmetrically within this set. When the two actuators operate at different amplitudes or phases, the microrobot can achieve clockwise or anticlockwise turns. The turning speed and radius can be controlled by adjusting the driving signals of the actuators. The mass of each component is presented in Supplementary Table 1.

Considering the extra mass of onboard power and control units for untethered locomotion, two different buoyancy mechanisms are employed to support the whole body of the microrobot on the water surface. Fig. 1d shows the water strider floating on the water surface via the tension from the long legs. In addition to surface tension, whirligig beetles employ partial body submersion as an alternative mechanism to produce supplemental buoyancy, which obviates the necessity of elongated legs[3,33]. Inspired by that, the microrobot also simultaneously employs surface tension from the floating pads and body buoyancy from the buoyancy

tank to achieve flotation on the water surface, as shown in Fig. 1e. Furthermore, the four floating pads are connected via an X-shaped beam to establish the requisite stability of the microrobot on the water surface.

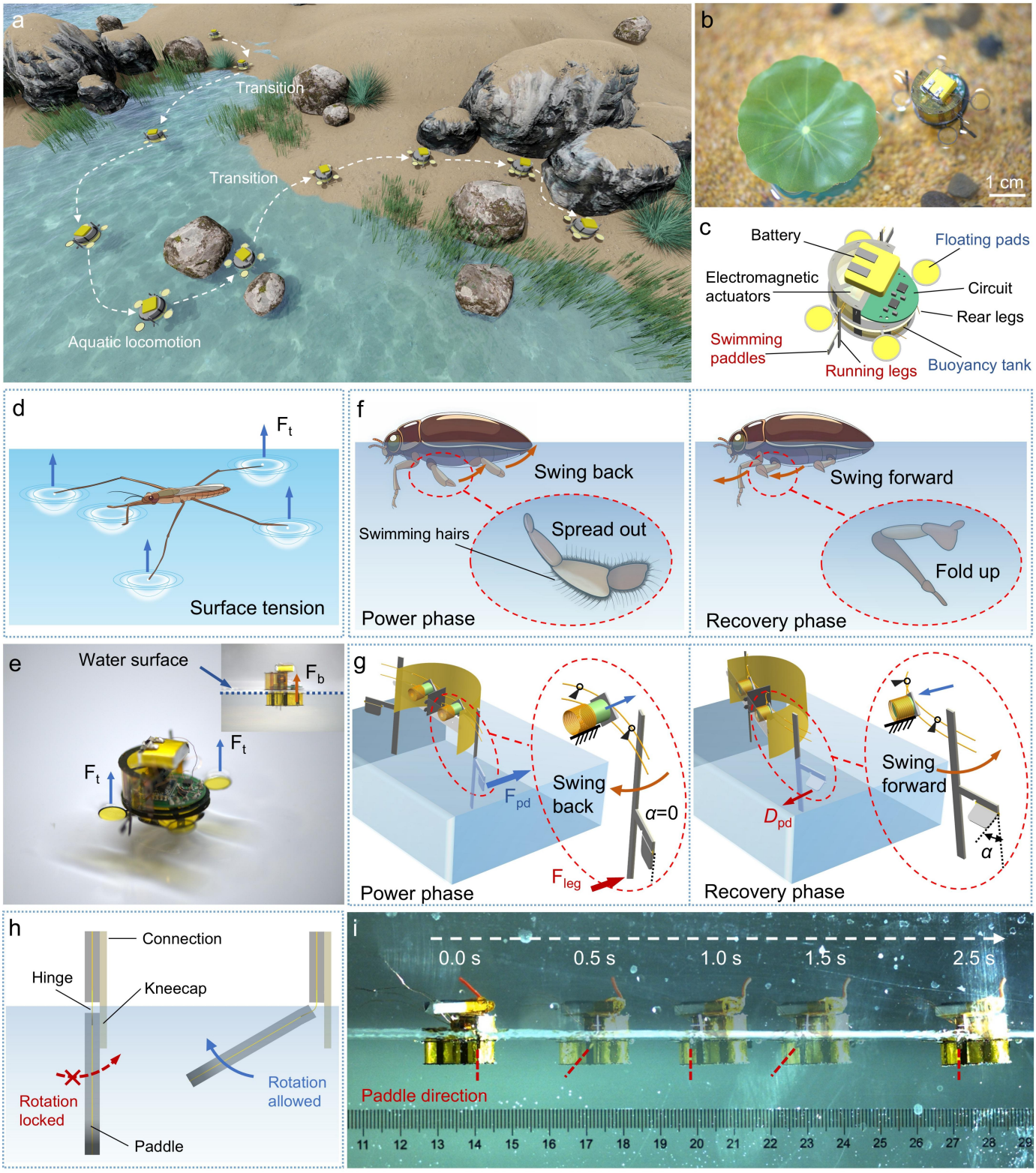


Fig. 1. Structural design and asymmetric vibration pattern of the microrobot. a, Locomotion scene diagram of the microrobot in an amphibious environment, including forward movements/turns on water surface and ground, as well as bidirectional transitions between water surface and ground. **b,** Optical photo of an untethered microrobot integrated with a lithium battery and an onboard power and control circuit. **c,** Three-dimensional model to show the structural details of the microrobot. **d,** Schematic diagrams illustrating the buoyancy mechanisms of water striders on the water surface. **e,** Hybrid buoyancy mechanism employed by the microrobot: surface tension from the floating pads and buoyancy from the buoyancy tank. **f,** Diagrams illustrating the swimming mechanism of the whirligig beetle, based on alternating power and recovery phases. A larger propulsion area is achieved during the

power phase due to expansion of the middle/hind legs and leg hairs. **g,** Diagrams illustrating the similar mechanism of propulsion generation for the microrobot on the water surface through the asymmetric vibration of the swimming paddle, which comprises a power phase and a recovery phase in each cycle. Unidirectional passive hinge enables backward-only rotation of the swimming paddle, yielding a larger propulsive area during the power phase. **h,** Enlarged schematic showing the operation mechanism of the swimming paddle with the unidirectional passive hinge. **i,** High-speed image showing the swimming locomotion of the microrobot, with the swimming paddle executing asymmetric vibration.

To reduce the number of necessary actuators required while achieving rapid locomotion on both land and water, we propose an asymmetric vibration pattern that drives an integrated actuation mechanism composed of a running leg and a swimming paddle. The running leg is designed to be longer than the rear supporting leg, thereby tilting the body at a specific angle. During terrestrial locomotion, the tilt-induced asymmetry in leg vibration defines a power phase during the backward swing, in which the leg impacts the ground to produce propulsion; and a recovery phase during the forward swing, in which the leg swings through air with reduced drag. Consequently, a net propulsion force is generated within each vibration cycle, driving microrobot to move forward on the ground. As the vibration frequency of the running legs approaches the resonant frequency of the microrobot, the propulsive force becomes sufficient to induce periodic airborne phases, thereby enabling an ultrafast running gait[7,34].

To achieve agile aquatic locomotion, the microrobot also employs the asymmetric vibration generated by the swimming paddle, similar to that observed in whirligig beetles. As shown in Fig. 1f, one swimming cycle of a whirligig beetle consists of a power phase and a recovery phase. During the power phase, the middle and hind legs with “swimming hairs” of whirligig beetles can spread out under pressure and swing backwards, which results in a large contacting area and propulsion force. In contrast, middle and hind legs fold via joints to reduce contacting area and damping force during the recovery phase [3,33]. Inspired by that, a swimming paddle with a unidirectional passive hinge is designed to generate asymmetric vibrations on the water surface, thereby achieving a similar swimming mechanism. As shown in Fig. 1g, the front leg is connected with two simply supported beams, which can be excited to vibration by the linear electromagnetic actuator. The operation mechanism of the swimming paddle under actuation of the actuator is shown in Fig. 1h. During the recovery phase, the front leg swings forward, and the swimming paddle swings backward around the

unidirectional passive hinge under water damping force, which leads to a relative deviation angle α. During the power phase, the front leg swings backwards, and the swimming paddle swings forwards until α drops to zero due to the limitation of the unidirectional passive hinge (Fig. 1h). Therefore, the contact area of the paddle in power phase is larger than that in recovery phase, resulting in a net propulsion force to drive the microrobot swimming forward. To demonstrate the swimming mechanism, a tethered prototype was fabricated for aquatic locomotion test. The detailed description of the fabrication process is available in Materials and Methods, and Supplementary Fig. 1. As shown in Fig. 1i and Supplementary Movie 1, it is observed that the swimming paddle rotates around the hinge asymmetrically during the aquatic locomotion.

Tethered aquatic locomotion performance

The aquatic locomotion performance of microrobot is determined by the net propulsion force during the power phase and recovery phase. Based on the swimming mechanism analysis, the net propulsion force correlates with the difference in contact area between the power and recovery phases, which is a function of the maximum relative deviation angle α_{max} and the area of the paddle A_{pd}. To improve the aquatic locomotion performance of microrobot, several key structural parameters of the paddle are selected to investigate the influence, including the geometric dimensions of the paddle (width w_{pd} and height h_{pd}), the thickness of the passive hinge (t_{hg}), and the relative height between the hinge and water surface (h_{hg}).

Figure 2a depicts the variations of the relative aquatic speed versus the actuating frequency under three sets of geometric dimensions of the paddle. For any set of geometric dimensions, the relative aquatic speed of the microrobot reaches its maximum near the resonance frequency, at which point angle α_{max} also attains its peak value (Supplementary Fig. 2). Furthermore, it is observed that an intermediate paddle size (3 mm ×2 mm) yields a superior moving speed. Under a large paddle size, the decrease in angle α_{max} predominates, resulting in a diminished speed at resonance. In contrast, the decrease in area A_{pd} predominates under a small paddle size, which also results in dropping of the aquatic speed.

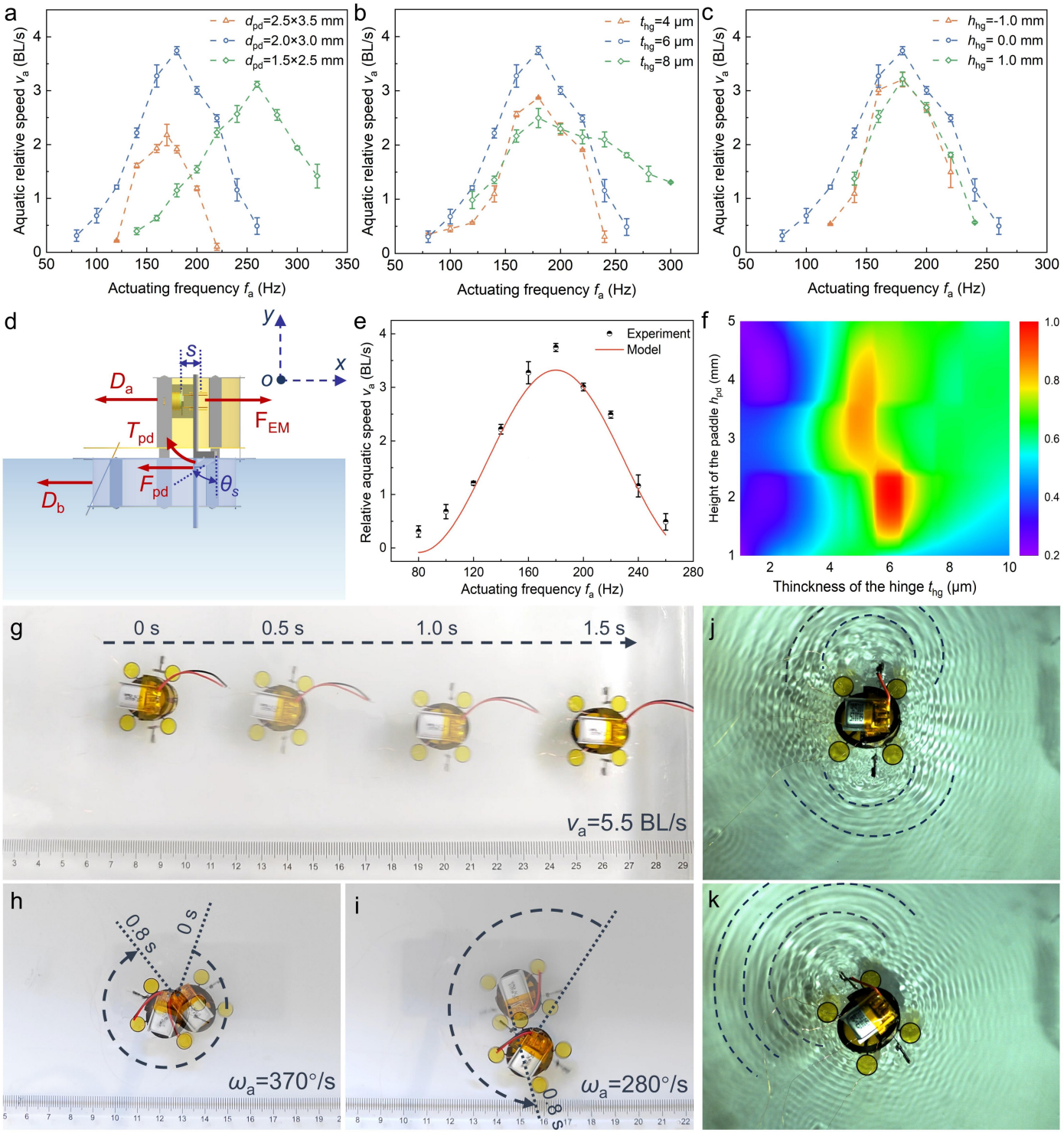


Fig. 2. Parameter design and tethered aquatic locomotion of the microrobot. a, Measurements of the relative aquatic speeds of three prototypes with different paddle dimensions (2.5 mm×1.5mm, 3.0 mm×2.0 mm, and 3.5 mm×2.5 mm) versus the actuating frequency, with the current amplitude remaining constant. **b,** Measurements of the relative aquatic speeds of three prototypes with different hinge thicknesses (4 μm, 6 μm, and 8 μm) versus the actuating frequency, with the current amplitude remaining constant. **c,** Measurements of the relative aquatic speeds of three prototypes with different relative heights of the hinge (-1.0 mm, 0.0 mm, and 1.0 mm) versus the actuating frequency, with the current amplitude remaining constant. **d,** Simplified dynamical model of the microrobot to analyze the aquatic locomotion characteristics. **e,** Experimental and simulation results of the relative aquatic speed of the microrobot versus the actuating frequency. **f,** Simulation results of normalized relative aquatic speed versus the height of the paddle h_{pd} and the thickness of the passive hinge t_{hg}. **g,** Optical photo of the tethered microrobot swimming forward with a relative speed of 5.5 BL/s when carrying a lithium battery (1200 mg). **h, i,** Optical photos of the microrobot achieving clockwise and anticlockwise turns on the water surface with a maximum turning speed of 370°/s and 280°/s respectively when carrying a lithium battery (1200 mg). **j, k,** Water surface waves generated by the microrobot during straight locomotion and clockwise turning. All error bars represent the standard deviation of three measurements.

The thickness of the passive hinge also exerts a significant influence on the aquatic locomotion performance, which determined the torsional stiffness of the paddle, as shown in Fig. 2b. There also exists an optimal hinge thickness at which the microrobot achieves its maximum aquatic speed. Similar to a large paddle size, a larger thickness t_{hg} also results in a smaller angle α_{max} because of the high torsional stiffness of the paddle, leading to a lower locomotion speed. At a smaller thickness t_{hg}, it is observed that the swimming paddle achieves a larger angle α_{max} during the recovery phase, but fails to return to 0° during the power phase in every other actuation cycle (Supplementary Fig. 3). Consequently, the average angle α_{max} throughout the locomotion process is reduced relative to that under an optimal hinge thickness, which also degrades the locomotion speed. Fig. 2c depicts the frequency response characteristics of the relative aquatic speed under different height h_{hg}, which determines the contact area between the swimming paddle and water. When h_{hg} is equal to 0 (the hinge axis lies at the waterline), the microrobot can realize the largest propulsion area and the highest relative aquatic speed.

To conduct parameters optimization for improving the aquatic locomotion performance, a simplified dynamic model of microrobot is established, as shown in Fig. 2d. It is assumed that two electromagnetic actuators are driven by the same current signals, resulting in purely linear forward motion of microrobot. Under this assumption, the microrobot is simplified as a system composed of two rigid bodies (M_f and M_{pd}) and a lumped mass (m_e). M_f represents the relatively stationary parts of the microrobot (such as the support frames and buoyancy tank), and M_{pd} represents the swimming paddle. The lumped mass m_e corresponds to the equivalent of the permanent magnet and the simply supported beams within the electromagnetic actuator. The hinge connecting M_f and M_{pd} is simplified as a unidirectional torsional spring. Three generalized coordinates are selected to establish the dynamic equations of the microrobot, including the translational displacement of M_f (x), the relative linear displacement of the concentrated mass m_e (s), and the relative angular displacement of M_{pd} (θ_s). The detailed discussion is shown in Supplementary Note 1.

The performance characteristics of the microrobot can be evaluated based on the above dynamic model, such as the frequency response characteristics of the aquatic relative speed. As shown in Fig. 2e, the simulation trend aligns closely with the experimental data, validating the dynamic model. Based on the dynamic model, the paddle parameters are optimized for enhanced aquatic speed. The height of the paddle (h_{pd}) and the thickness of the passive hinge (t_{hg}) are selected as the design parameters to be optimized, with the width of the paddle w_{pd} constrained to maintain a constant proportion to h_{pd}. Fig. 2f shows the normalized aquatic speed map of the microrobot. The color bar represents the magnitude of the normalized aquatic speed, with the red color area indicating the fastest speed. It is found that h_{pd} near 2.0 mm and t_{hg} near 6.0 μm are the optimal values for achieving the fastest aquatic speed.

To demonstrate the enhanced aquatic speed compared to the original prototype, one optimized prototype microrobot with optimized parameters was fabricated. During the aquatic locomotion test, a lithium battery (1200 mg) is mounted onboard the prototype but remains electrically disconnected, emulating the functional payloads required for untethered locomotion. Fig. 2g shows the optimized prototype swimming forward with a maximum speed of 11.5 cm/s (5.5 BL/s, Supplementary Movie 2), surpassing the performance of the initial prototype at 3.7 BL/s (Supplementary Movie 2). Benefiting from two independent actuators, the microrobot can also realize clockwise or anticlockwise turns with only one actuator activated. Fig. 2h and 2i show the prototype achieving the maximum turning speeds of 370°/s in the clockwise turning with a radius of 1.0 cm and 280°/s in the anticlockwise turning with a radius of 1.5 cm (Supplementary Movie 3).

To investigate the fast aquatic moving mechanism, a high-speed imaging system is utilized to capture the water-surface morphologies during the aquatic forward and turn movements. During the reciprocating motion of the swimming paddle, it produces surface waves that radiated outward across the water surface. Owing to the unidirectional passive hinge, the swimming paddle vibrates asymmetrically near the water surface, resulting in differential wave amplitudes in the forward and backward directions. To facilitate observation of the surface waves, the microrobot under single-actuation mode is examined first. As shown in Supplementary

Fig. 4, with the paddle oscillation frequency approaching the resonant frequency of the microrobot, the wave amplitude in the forward direction gradually decreases. The decrease indicates a reduction in the force exerted by the paddle on the water surface in the forward direction, and consequently a decrease in the backward reaction force from the water onto the paddle. In contrast, the wave amplitude in the backward direction exhibits no discernible change. The resulting net propulsive force therefore increased with frequency increasing, revealing the hydrodynamic mechanism by which the microrobot achieves its maximum speed near the resonant frequency.

A further comparison is made between the optimized and original prototypes regarding their free-surface wave behavior near resonance. Relative to the initial prototype, the optimized prototype exhibits markedly more vigorous and even fragmented surface waves at the backward direction as the paddle actuation frequency approaches the resonance frequency of the microrobot, thereby enabling significantly enhanced propulsive effect and aquatic speed.

Controlled untethered aquatic locomotion

Operation in most natural environments requires the amphibious microrobots to be untethered. Owing to the challenge of integrating onboard power units at small scales, untethered locomotion remains a major challenge of amphibious microrobots. Benefiting from the low operation voltage of the linear electromagnetic actuators and the reduced demand of voltage signals inherent to a unified amphibious actuation mechanism, the onboard power electronics of microrobot can be substantially miniaturized. Fig. 3a shows a compact power and control circuit with two independent voltage signals (555 mg, 17.5 mm × 14.5 mm). The circuit is arranged in an elliptical pattern to match the profile of the microrobot. A wireless embedded microprocessor is utilized to receive remote control instructions and adjust the frequency of the output voltage signals. The mass and quantity of the electrical components used in the circuit are shown in Supplementary Table 2.

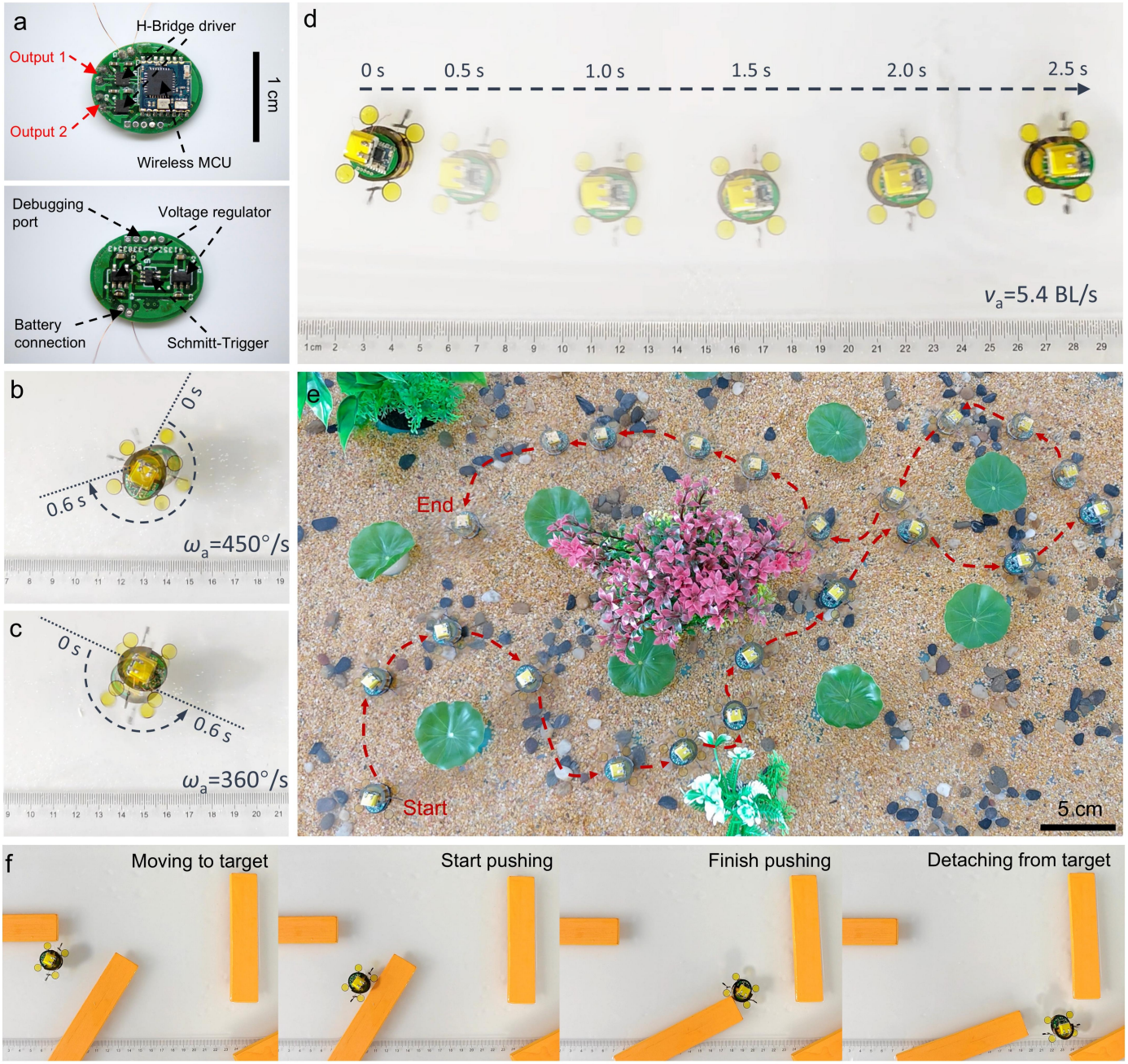


Fig. 3. Controlled untethered aquatic locomotion of the microrobot. a, Top view and bottom view of the power and control circuit board. **b, c,** Optical photos of the microrobot achieving clockwise and anticlockwise turns on the water surface with a maximum turning speed of 450°/s and 360°/s respectively. The red dotted lines represent the angular displacements of the microrobot in 0.6 s. **d,** Optical photo of the microrobot swimming linearly on the water surface with a maximum speed of 5.4 BL/s. The red dotted lines represent the locomotion displacements of the microrobot in 2.5 s. **e,** The scenario of the microrobot crossing a 100 cm-by-60 cm water pool scattered with simulated aquatic plants and lotus leaves under remote control, then returning to the starting point along a different path. **f,** Optical photos of the microrobot approaching, pushing away, and detaching from floating wooden blocks that are 6.6 times heavier than the microrobot itself.

Based on the circuit, an untethered microrobot was fabricated to demonstrate controlled and untethered amphibious locomotion, including clockwise/anticlockwise turns and straight forward motion. On the water surface, the microrobot can achieve a maximum turning angular speed of 450°/s in the clockwise direction and 360°/s in the anticlockwise direction, as shown in Fig. 3b and 3c (Supplementary Movie 4). Fig. 3d shows

252 that the microrobot can achieve a maximum straight moving speed of 5.4 BL/s on the water surface
253 (Supplementary Movie 4).

254 Under remote control instructions, the microrobot is capable of traversing complex water surface
255 environments cluttered with numerous obstacles by employing two distinct strategies: navigating around
256 immovable obstacles or pushing away lightweight floating obstacles in the path. A simulated water pool (100
257 cm by 60 cm) was constructed to evaluate the obstacle avoidance capability of the microrobot (Fig. 3e). To
258 emulate a natural cluttered water surface, simulated lily pads and aquatic plants were distributed throughout
259 the pool as obstacles. The microrobot successfully navigated around the simulated lily pads and aquatic plants,
260 traversing from the lower left corner to the upper right corner of the pool, with red dotted lines representing
261 the moving trajectory. Subsequently, the microrobot returned to the left side of the pool via a distinctly
262 different trajectory. During the entire traversal, a total of 31 turning maneuvers and 32 straight forward
263 movements are executed by the microrobot (Supplementary Movie 5).

264 The microrobot can adopt an alternative strategy to traverse an obstacle by pushing it away directly,
265 provided the obstacle is lightweight. In this scenario, several wooden blocks floating on the water surface are
266 placed in the forward path of the microrobot. Fig. 3f shows that the microrobot successfully pushed away a
267 wood block weighing 6.6 times (11.3 g) its own body weight. Once the passage is cleared, the microrobot can
268 detach from the wood block via a sequence of turning and forward movements (Supplementary Movie 6).

269 **Terrestrial locomotion performance**

270 Terrestrial locomotion speed constitutes an equally important aspect in assessing the overall performance
271 of an amphibious microrobot. A simplified dynamic model (see Supplementary Note 2 and Supplementary
272 Fig. 5) is also established to investigate the influencing factors of the terrestrial locomotion performance of
273 microrobot, including the frequency (f_a) and amplitude (I_a) of the current signals applied to the actuators, and
274 the payload mass (m_p). A plastic board is employed as a substrate to evaluate the terrestrial locomotion
275 performance of the microrobot.

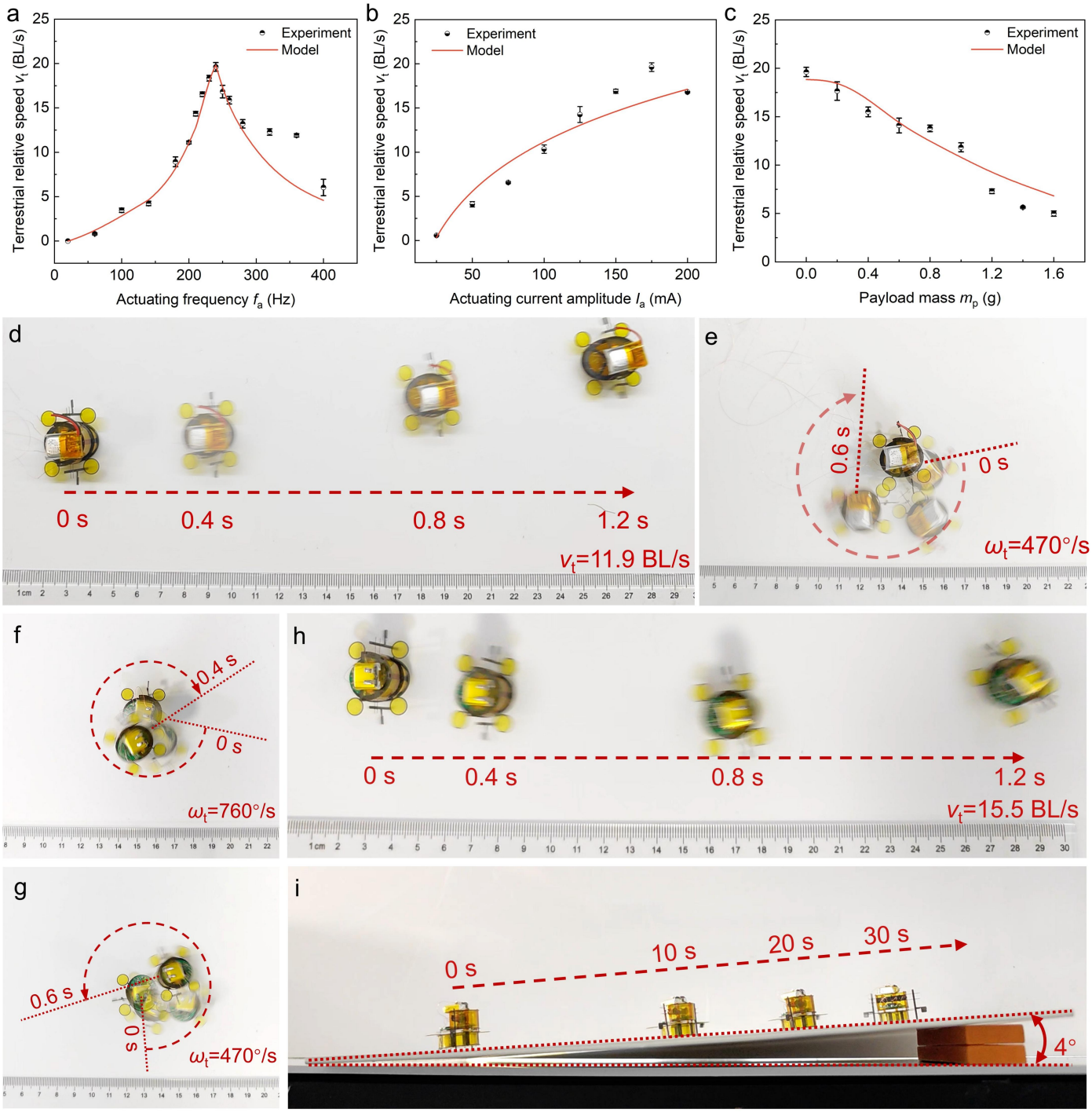


Fig. 4. Terrestrial locomotion performance of the microrobot. a, Experimental and simulation results of the relative terrestrial speed of the tethered microrobot versus the actuating frequency. **b,** Experimental and simulation results of the relative terrestrial speed of the tethered microrobot versus the actuating current amplitude. **c,** Experimental and simulation results of the relative terrestrial speed of the tethered microrobot versus the payload mass. All error bars represent the standard deviation of three measurements. **d,** Optical photo of the tethered microrobot moving forward with a relative speed of 11.9 BL/s on a plastic board when carrying a lithium battery (1200 mg). **e,** Optical photo of the tethered microrobot achieving clockwise turning on the plastic board with a maximum turning speed of 470°/s under a payload mass of 1200 mg. **f, g,** Optical photos of the untethered microrobot achieving clockwise and anticlockwise turns on a plastic board with a maximum turning speed of 760°/s and 470°/s respectively. **h,** Optical photo of the untethered microrobot running linearly on the plastic board with a maximum speed of 15.5 BL/s. **i,** Optical photo showing the untethered microrobot moving on a slope of 4° via a bipedal alternating relay climbing strategy.

Similar to aquatic locomotion, experimental and simulation results both indicate that the microrobot attains its maximum terrestrial speed near the resonance frequency on the plastic board (as shown in Fig. 4a), which

differs with that on the water surface. Fig. 4b shows the experimental and simulated variation trend of the terrestrial speed versus I_a, which increases generally with the increase of I_a. However, as I_a continues to rise, the terrestrial speed began to decline instead, due to the saturation of the electromagnetic driving force.

Given that task execution typically requires the microrobot to transport functional payloads, characterizing the effect of payload mass on locomotion performance is essential. Throughout the characterization process, I_a remains constant (0.15 A) for a given payload mass. The frequency f_a is swept to identify the resonance frequency corresponding to the payload mass, from which the maximum attainable speed is subsequently derived. Fig. 4c shows the experimental and simulated maximum attainable locomotion speeds as the payload mass varied from 0 mg to 1600 mg. The progressive increase in friction results in a decline of the peak speed of the microrobot near resonance as the payload mass rises. Supplementary Fig. 6a shows the microrobot can achieve a maximum relative speed of 19.5 BL/s under a payload of 0 mg (0.15A), while the speed drops to 7.3 BL/s under a payload of 1200 mg, which is the estimated mass of the power and control units for untethered locomotion. Furthermore, an elevated current amplitude contributes to an improved locomotion speed of the microrobot when subjected to a large payload mass. When the current amplitude rises to 0.2A, the microrobot can achieve a maximum relative speed of 11.9 BL/s under a payload of 1200 mg, as shown in Fig. 4d and Supplementary Movie 7.

Similar to aquatic locomotion, the microrobot can also realize agile clockwise/anticlockwise turns by switching the activation of two independent actuators. On a plastic board, the microrobot demonstrates a maximum turning angular speed of 580°/s in the clockwise direction and 570°/s in the anticlockwise direction under a payload of 0 mg, as shown in Supplementary Fig. 6b, S6c and Supplementary Movie 8 (0.15 A). Under a payload of 1200 mg, the microrobot can also achieve a maximum clockwise turning speed of 470°/s, as shown in Fig. 4e and Supplementary Movie 8 (0.20 A). The anticlockwise turn of the microrobot under a payload mass of 1200 mg is shown in Supplementary Fig. 6d.

The microrobot integrated with the power and control units can also accomplish fast running movements on the ground. A plastic board is utilized to investigate the terrestrial locomotion performance of the microrobot. Fig. 4f and 4g shows the microrobot achieving a maximum turning angular speed of 760°/s in the clockwise direction and 470°/s in the anticlockwise direction (Supplementary Movie 9). When two electromagnetic actuators are both activated, the microrobot achieved a maximum straight forward running speed of 15.5 BL/s, as shown in Fig. 4h and Supplementary Movie 8.

As the terrain in practical scenarios tends not to be flat, the slope-climbing performance of the microrobot has also been evaluated. Due to the additional weight introduced by the power and control units, sustained uphill locomotion is difficult to achieve for the microrobot with two actuators activated. Accordingly, a bipedal alternating relay climbing strategy is introduced for slope-climbing. It is observed that diagonally upward movements with short distance on a slope can be achieved by the microrobot with only one front leg actuated. Therefore, the microrobot can realize continuous slope climbing by sequentially activating the actuators of the left front leg and the right front leg. As shown in Fig. 4i and Supplementary Movie 10, the untethered microrobot demonstrated a 4° slope ascent within 30 s.

Transitions between water and land

Transitions between water and land constitutes a critical requirement for amphibious microrobots. While the amphibious microrobot is capable of terrestrial and aquatic locomotion independently, the key challenge resides in the transition across the transitional boundary between water and land, which is actually another new terrain.

When traversing the boundary region, the microrobot inevitably enters or exits the water surface, and thus frequently operates in a partially submerged state. Therefore, mobility evaluation is essential for amphibious microrobots under these partially submerged, hydrodynamically loaded conditions. Supplementary Fig. 7a and 7b show the generated propulsion force of the microrobot in a partially submerged state with different submergence depths (3 mm and 6 mm). As submergence depth increases, the forward locomotion of the

microrobot transitions from the foreleg-only propulsion to a combined foreleg-paddle propulsion, because the paddle immerses progressively into the water (Supplementary Fig. 7c). Furthermore, increased submergence depth introduces two competing effects: reduced leg-ground frictional resistance resulting from enhanced buoyancy, and elevated hydrodynamic drag.

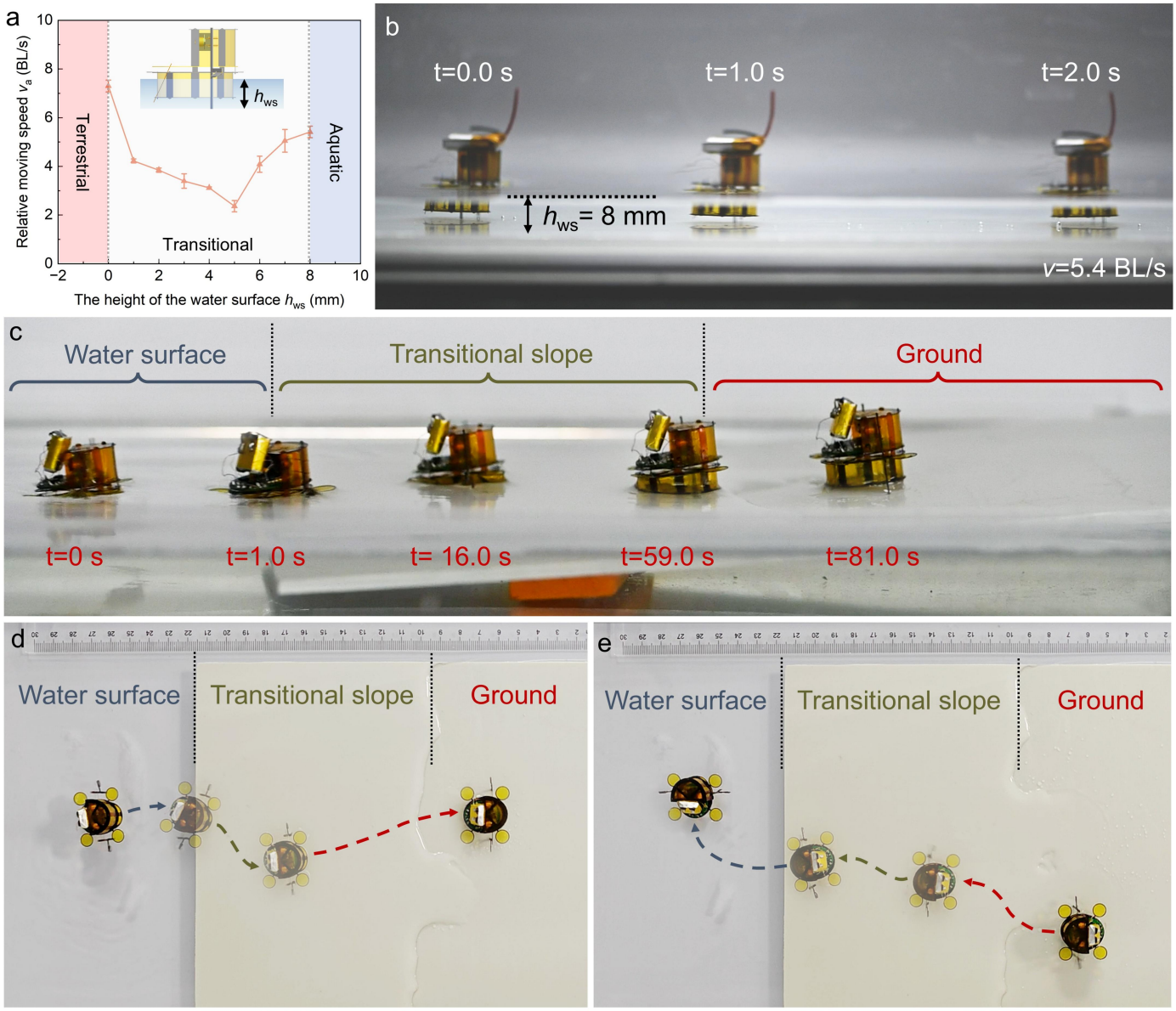


Fig. 5. Transitions between water and land for the microrobot. a, Measurements of the relative speed of the microrobot versus the height of the water surface in a partially submerged state. All error bars represent the standard deviation of three measurements. **b,** Optical photo of the tethered microrobot moving forward at a maximum speed of 5.4 BL/s at a submersion depth of 8 mm, with the front leg and swimming paddle jointly generating propulsion. **c,** Side view showing the untethered microrobot continuously traversing water surface, water-land transition, and ground in 81.0 s via a transitional slope. **d, e,** Overhead view showing the untethered microrobot continuously transitioning from water to ground and from ground to water.

A water pool (60 cm × 40 cm) is employed to characterize the locomotion performance of the microrobot under varying submergence depth. As shown in Fig. 5a, the relative moving speed reaches a minimum at an intermediate water level (5 mm) before recovering, with increasing submergence depth. The initial decline in

speed at lower submergence depths can be attributed to the predominance of increasing hydrodynamic drag. Beyond a critical submergence depth, the speed begins to rise, resulting from the friction reduction and the extra thrust generated by the swimming paddles. At the maximum submergence depth of 8 mm, the microrobot can achieve a locomotion speed of 5.4 BL/s (Fig. 5b and Supplementary Movie 11).

We further investigate how the microrobot crosses the water–land boundary under a partially submerged state completely, starting from either water surface or land. Since shorelines in natural environments are often sloped, a partially submerged slope is adopted as a simplified experimental scenario. Constrained by size limitations, amphibious microrobots face considerable difficulty in developing effective locomotion strategies specifically for the sloped boundary. Benefiting from the capabilities of water traversal and slope ascent, the microrobot is capable of accomplishing the water-land transitions via the partially submerged slope, where the microrobot can employ the bipedal alternating relay climbing strategy. Fig. 5c shows the lateral aspect of the water-to-land transition, depicting the microrobot swimming on the water surface, then traversing the submerged slope, and eventually emerging onto the terrestrial plane. Subsequently, the microrobot reversed its orientation, descending from the terrestrial plane back to the water surface. A complete bidirectional water-land transition cycle is recorded by Fig. 5d and 5e (overhead view) and Supplementary Movie 12.

Discussion

We demonstrated here an insect-scale (2.1 cm, 1.69 g), untethered, and controlled amphibious microrobot with high agility on both water surface and ground. The microrobot employs an asymmetric vibration pattern for amphibious locomotion, realized by two symmetrically arranged actuation mechanisms, each integrating a running leg and a swimming paddle. When two actuators are activated simultaneously, the microrobot can realize both fast untethered straight locomotion on the water surface (5.4 BL/s) and ground (15.5 BL/s). Rapid turning with small radius is realized by driving only one actuator, thereby generating asymmetric propulsion for steering. The maximum turning speeds of the untethered microrobot on the water surface and ground are separately 450°/s and 760°/s. Furthermore, the untethered microrobot can also achieve bidirectional

transitions between the water surface and ground via a slope. To further compare the locomotion performance of the microrobot with that of other insect-scale amphibious microrobots quantitatively, we select relative linear running speed and energy conversion efficiency as two performance indicators.

Owing to size constraints, existing amphibious microrobots are typically powered by external power sources or energy fields. Even with the integration of onboard power and control units, the mobility of the microrobots remains limited in terrestrial or aquatic environments, owing to the high ground friction or hydrodynamic drag. Fig. 6a and 6b presents the comparison of the relative moving speed with respect to the body length for several amphibians[35-38] (blue triangles), reported untethered amphibious robots[12,14,17,19,22,23,26,28,39-45] (orange circles), reported tethered amphibious robots[20,24,25,27,31,32,46-54] (purple diamonds), and the microrobot (red pentagram). Detailed data for performance comparison is provided in Supplementary Table 3.

Based on the comparisons, it is concluded that the untethered microrobot achieves the minimal dimension among existing tethered and untethered robots, while exhibiting superior locomotion agility across both aquatic and terrestrial environments, even when scaled to a body length of 1 m. In particular, we perform a comprehensive comparison of the microrobot with several other amphibious microrobots (body length < 6.0 cm) presented in recent years, as shown in Table 1. The microrobot is the only insect-scale untethered system that achieves complete wireless controlled amphibious locomotion. When comparing with amphibians, the microrobot also outperforms larger species (such as green turtles) in aquatic and terrestrial locomotion agility, matching the performance of those with similar size (Lizard, *Anolis Sagrei*, 5 cm).

Table 1. Comparison of this work and other amphibious microrobots with body length less than 6.0 cm.

Robot description	Body length (mm)	Total mass (g)	Terrestrial speed (BL/s)	Aquatic speed (BL/s)	Untethered	Controlled	Aquatic–terrestrial transition
This work	21	1.69	15.5	5.4	Yes	Yes	Bidirectional
HAMR[27]	40	1.6	1.75	0.7	No	Yes	Bidirectional
Leglessbot[28]	55	24.0	1.4	0.61	Yes	Yes	Unidirectional
SAM[25]	45	1.4	3.4	2.02	No	Yes	Unidirectional
AISR[54]	44	1.66	2.44	1.2	No	No	Bidirectional

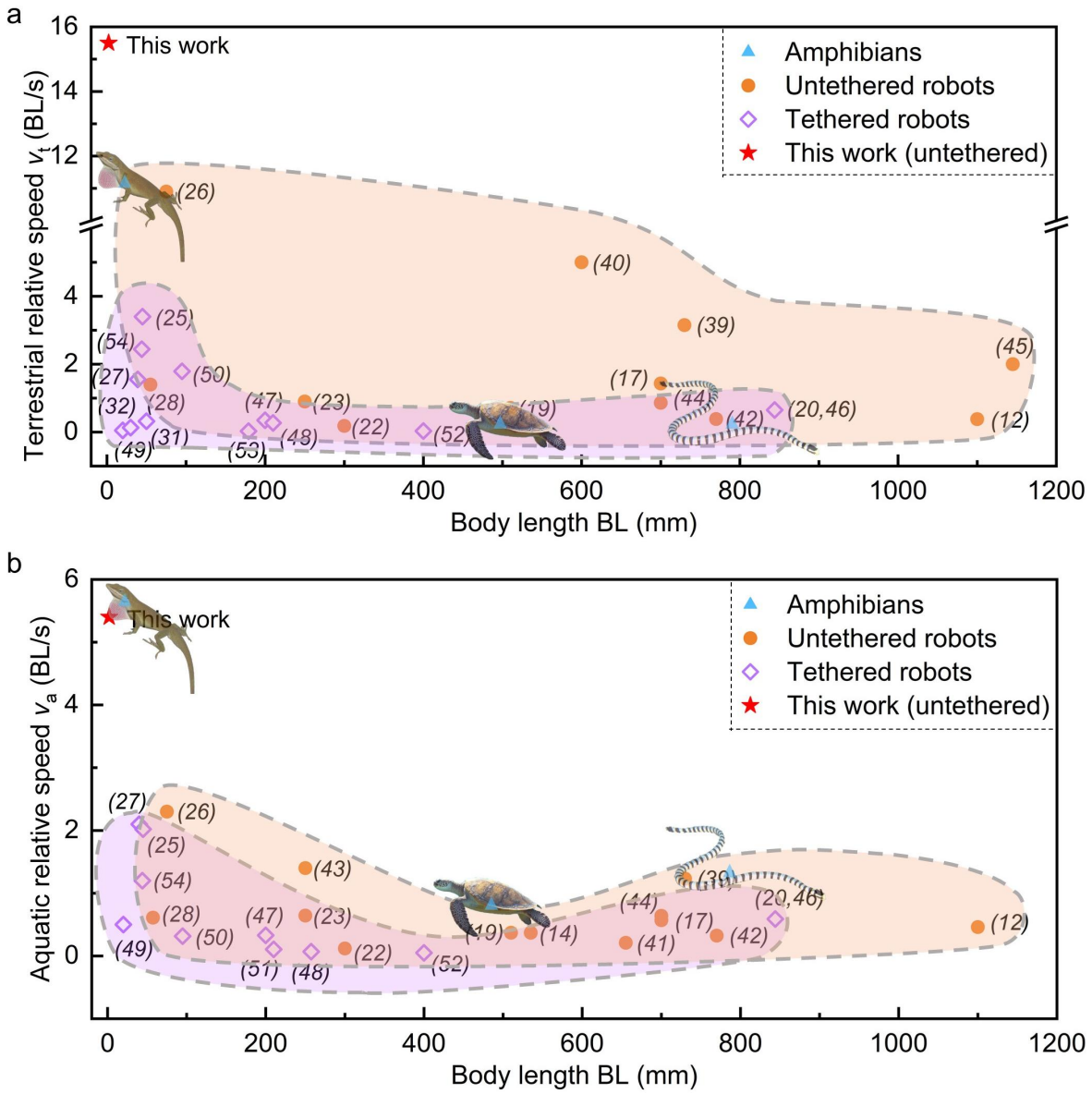


Fig. 6. Locomotion performance comparison of the microrobot with natural creatures and other amphibious robots. a, Comparison of terrestrial relative speed versus the body length with selected amphibious creatures (blue triangles), tethered amphibious robots (purple diamonds), untethered amphibious robots (orange circles) and the untethered microrobot (red pentagram). **b,** Comparison of aquatic relative speed versus the body length with selected amphibious creatures (blue triangles), tethered amphibious robots (purple diamonds), untethered amphibious robots (orange circles) and the untethered microrobot (red pentagram).

The energy conversion efficiency of the microrobot during aquatic or terrestrial locomotion is evaluated using the cost of transport (CoT), which is defined as:

$$\mathrm{CoT} = \frac{P_{\mathrm{in}}}{mgv} \tag{4}$$

where P_{in} is the power input of the onboard battery for the untethered prototype, m is the total mass (1.69 g), g is the standard gravity, and v is the moving speed on the water surface or the ground. During the aquatic locomotion, the maximum speed of the microrobot is 11.3 cm/s, with a total power consumption of 1.976 W (3.8 V, 0.52 A). Therefore, the CoT value is calculated to be 1056. During the terrestrial locomotion, the

maximum speed of the microrobot is 32.5 cm/s. Therefore, the CoT value is calculated to be 367. The CoT of the microrobot is higher than the HAMR driven by piezoelectric actuators (83.9 for terrestrial locomotion[55]), which is primarily influenced by the large current flowing through the circuit board and the low actuation efficiency of the electromagnetic actuators. Considering that the presented asymmetric vibration pattern and actuation mechanism in this work is also applicable to other linear actuators, it offers a promising route for other insect-scale legged microrobots.

Future research will focus on improving adaptability of the microrobot to unstructured terrestrial terrains (such as sand, muddy ground, and grassy surfaces) by developing adaptive structural designs of the front leg within the unified actuation mechanism. In addition, integrating an onboard visual sensing system and developing autonomous locomotion control strategies are critical to elevating the operational capability of the microrobot in real unstructured amphibious environments.

Method

Fabrication of the microrobot

The microrobot features a modular architecture, including the unified actuation mechanism for crawling and swimming, the main body, buoyancy tank, linear electromagnetic actuators, rear legs, and floating pads. Most modules are fabricated via laser cutting (Han's Laser UV3C, 3 W in power, and 355 nm in wavelength, China) and manual assembly, as shown in Supplementary Fig. 1.

The unified actuation mechanism consists of a front leg and a swimming paddle, which is fabricated through a laser micromachining and lamination process (SCM, smart composite microstructures)[56]. It is monolithically released from a single laminate composed of seven layers via laser cutting (Supplementary Fig. 1A), including three 150-μm-thick carbon fiber layers, three 12.5-μm-thick adhesive layers, and a 6-μm-thick polyimide layer (Supplementary Fig. 1B). The rear legs are made of Ni-Ti alloy wire with a diameter of 120 μm. Two prototypes of the unified actuation mechanism with different dimensions are presented in Supplementary Fig. 1C.

Both the main body and the buoyancy tank consist of three support frames. The frames are all laminated by an inner supporting layer cut from 150-μm-thick carbon fiber plates, an intermediate bonding layer cut from 12.5-μm-thick adhesive films (DuPont™ Pyralux® LF1500), and an outer waterproofing layer cut from 20-μm-thick polyimide films (DuPont™ Kapton® CR). The side supporting frame is first shaped into a curved profile to minimize hydrodynamic drag, and then glued with the top and bottom frames together with the assistance of mounting holes and flanges to ensure installation accuracy, as shown in Supplementary Fig. 1D.

The linear electromagnetic actuator consists of a hollow coil, a permanent magnet, two simply supported beams, and support frames. The permanent magnets (N52) and hollow coils wound by copper wire are both commercial products. The simply supported beams are made of Ni-Ti alloy wire with a diameter of 120 μm due to the high strength and low flexural rigidity. The support frames utilized to fix the hollow coil and permanent magnet are cut from 150-μm-thick carbon fiber plates.

The floating pad consists of four circular pads and an X-shaped beam, which is monolithically released from a laminate composed of three layers, including a 150-μm-thick carbon fiber layer, a 12.5-μm-thick adhesive layer and a 20-μm-thick polyimide layer. The hydrophobic polyimide layer is positioned at the bottom, directly contacting the water surface to generate surface tension.

Following fabrication of all constituent modules, the complete microrobot is manually assembled. Two symmetric linear electromagnetic actuators are fixed in the main body via the support frame of the hollow coil, with the simply supported beams extending out of the main body. Then, two actuation units are symmetrically glued on the simply supported beams. Next, the floating pad is glued on the buoyancy tank, sharing a common center point. Finally, the main body is fixed on the buoyancy tank with the assistance of mounting holes and flanges.

Power and control electronics

A power and control circuit with ellipse-shaped electronics substrate is designed to realize the untethered and controlled locomotion of the microrobot. The circuit comprises three functional modules: a voltage regulation unit, a control unit, and a power output unit. The voltage regulation unit incorporates two input pads for battery connection and two voltage regulators: one supplying 3.3 V to the control unit, and the other delivering 1.2 V to the power output unit. The control unit, based on the BLE SoC (Bluetooth low-energy system-on-chip; CC2640R2F, Texas Instruments), generates two PWM signals to control the power output unit. The power output unit consists of two H-Bridge drivers, a Schmitt-Trigger inverter, and four output pads. The four output pads can provide two independent voltage signals with variable frequencies. On the back side, there are two voltage regulators and a MEMS microphone. The surface of the PCB board is 143mm^2. The mass and quantity of the electrical components used in the circuit are shown in Supplementary Table 2.

Experimental setup for transition demonstration of water and land

To demonstrate the bidirectional transition between water surface and land, an experimental setup is constructed. The experimental setup comprises an acrylic tank (40 cm by 60 cm) to simulate the aquatic environment and a plastic board (20 cm by 30 cm) to serve as the ground. The plastic board is placed at a 5° incline within the acrylic tank. Its lower end is supported by a wooden block adhered to the tank floor, while its upper end rested on the rim of the tank, resulting in approximately half of its surface being submerged. The prototype microrobot is initially placed on the water surface at the left side of the tank. Guided by remote commands, the microrobot traversed from the water surface onto the emergent right side of the sloped plastic board, executed a 180° rotation, and subsequently returned from the plastic board to the water surface on the left side.

Measurement of power consumption

The power consumption of the microrobot is defined as the input power of the power and control circuit, which is powered by an onboard lithium battery (40 mAh). A 1-ohm resistor is inserted between the negative

side of the battery and the power and control circuit to measure the current. During the measurement, the robot remained stationary, yet the drive signal supplied by the circuit is identical to that used for achieving its maximum locomotion speed.

Statistical analysis

All data are expressed as either the means or the means ± standard deviation, unless specified differently. The number of samples is given in the figure captions.

Data availability

All data needed to evaluate the conclusions in the paper are present in the paper and/or the Supplementary Materials.

Code availability

The code used in this paper is available upon any reasonable request.

References

1 Hu, D. L., Chan, B. & Bush, J. W. M. The hydrodynamics of water strider locomotion. *Nature* **424**, 663-666, doi:10.1038/nature01793 (2003).

2 Yang, E., Son, J. H., Lee, S.-i., Jablonski, P. G. & Kim, H.-Y. Water striders adjust leg movement speed to optimize takeoff velocity for their morphology. *Nat. Commun.* **7**, 13698, doi:10.1038/ncomms13698 (2016).

3 Nachtigall, W. in *The Physiology of Insecta (Second Edition)* (ed Morris Rockstein) 381-432 (Academic Press, 1974).

4 Xu, Z., Lenaghan, S. C., Reese, B. E., Jia, X. & Zhang, M. Experimental Studies and Dynamics Modeling Analysis of the Swimming and Diving of Whirligig Beetles (Coleoptera: Gyrinidae). *PLoS Comput. Biol.* **8**, e1002792, doi:10.1371/journal.pcbi.1002792 (2012).

5 Fish, F. E. & Nicastro, A. J. Aquatic turning performance by the whirligig beetle: constraints on maneuverability by a rigid biological system. *J. Exp. Biol.* **206**, 1649-1656, doi:10.1242/jeb.00305 (2003).

6 Wu, Y. *et al.* Insect-scale fast moving and ultrarobust soft robot. *Sci. Rob.* **4**, eaax1594, doi:10.1126/scirobotics.aax1594 (2019).

7 Liu, Z. *et al.* A wireless controlled robotic insect with ultrafast untethered running speeds. *Nat. Commun.* **15**, 3815, doi:10.1038/s41467-024-47812-5 (2024).

8 Hartmann, F. *et al.* Highly agile flat swimming robot. *Sci. Rob.* **10**, eadr0721, doi:10.1126/scirobotics.adr0721 (2025).

9 Wu, Y. *et al.* Untethered soft microrobot driven by a single actuator for agile navigations. *Nat. Commun.* **16**, 6842, doi:10.1038/s41467-025-61810-1 (2025).

10 Yu, J. Z. *et al.* On a Bio-inspired Amphibious Robot Capable of Multimodal Motion. *Ieee-Asme T Mech* **17**, 847-856, doi:10.1109/Tmech.2011.2132732 (2012).

11 Baines, R. *et al.* Multi-environment robotic transitions through adaptive morphogenesis. *Nature* **610**, 283-289, doi:10.1038/s41586-022-05188-w (2022).

12 Crespi, A., Karakasiliotis, K., Guignard, A. & Ijspeert, A. J. Salamandra Robotica II: An Amphibious Robot to Study Salamander-Like Swimming and Walking Gaits. *IEEE Trans. Rob.* **29**, 308-320, doi:10.1109/TRO.2012.2234311

(2013).
13 Horvat, T. *et al.* in *2015 IEEE/RSJ International Conference on Intelligent Robots and Systems (IROS).* 195-201.
14 Wang, G. *et al.* Subsea crab bounding gait of leg-paddle hybrid driven shoal crablike robot. *Mechatronics* **48**, 1-11, doi:https://doi.org/10.1016/j.mechatronics.2017.10.002 (2017).
15 Kai, K., Nguyen, H. D., Wan, W. Y. & Sato, H. The Walking Control of a Crab Biorobot in Amphibious Environment. **11**, 596-605, doi:doi: 10.1089/soro.2023.0033 (2024).
16 Park, H. S. & Sitti, M. in *2009 IEEE/RSJ International Conference on Intelligent Robots and Systems.* 645-651.
17 Yang, Y., Zhou, G., Zhang, J., Cheng, S. & Fu, M. in *2015 IEEE/RSJ International Conference on Intelligent Robots and Systems (IROS).* 559-566.
18 Zhu, J. *et al.* in *2018 IEEE International Conference on Real-time Computing and Robotics (RCAR).* 417-420.
19 Zhong, B. *et al.* On a CPG-Based Hexapod Robot: AmphiHex-II With Variable Stiffness Legs. *IEEE/ASME Trans. Mechatron.* **23**, 542-551, doi:10.1109/TMECH.2018.2800776 (2018).
20 Zhang, S. *et al.* AmphiHex-I: Locomotory Performance in Amphibious Environments With Specially Designed Transformable Flipper Legs. *IEEE/ASME Trans. Mechatron.* **21**, 1720-1731, doi:10.1109/TMECH.2015.2490074 (2016).
21 Zhang, S., Liang, X., Xu, L. & Xu, M. Initial Development of a Novel Amphibious Robot with Transformable Fin-Leg Composite Propulsion Mechanisms. *J. Bionic Eng.* **10**, 434-445, doi:https://doi.org/10.1016/S1672-6529(13)60247-4 (2013).
22 Xing, H. *et al.* in *2019 IEEE/RSJ International Conference on Intelligent Robots and Systems (IROS).* 1702-1707.
23 Li, M., Guo, S., Hirata, H. & Ishihara, H. Design and performance evaluation of an amphibious spherical robot. *Rob. Auton. Syst.* **64**, 21-34, doi:https://doi.org/10.1016/j.robot.2014.11.007 (2015).
24 Wu, M. *et al.* A Fully 3D-Printed Tortoise-Inspired Soft Robot with Terrains-Adaptive and Amphibious Landing Capabilities. *Advanced Materials Technologies* **7**, 2200536, doi:https://doi.org/10.1002/admt.202200536 (2022).
25 Wu, G. *et al.* A piezoelectric driven amphibious microrobot capable of fast and controllable movement. *Smart Mater. Struct.* **33**, 115035, doi:10.1088/1361-665X/ad8610 (2024).
26 Wang, D. *et al.* Miniature Amphibious Robot Actuated by Rigid-Flexible Hybrid Vibration Modules. *Adv. Sci.* **9**, 2203054, doi:https://doi.org/10.1002/advs.202203054 (2022).
27 Chen, Y., Doshi, N., Goldberg, B., Wang, H. & Wood, R. J. Controllable water surface to underwater transition through electrowetting in a hybrid terrestrial-aquatic microrobot. *Nat. Commun.* **9**, 2495, doi:10.1038/s41467-018-04855-9 (2018).
28 Tang, L. *et al.* Inertia-driven amphibious robot with asymmetric microundulatory fin arrays. *Sci. Adv.* **12**, eaea2222, doi:10.1126/sciadv.aea2222 (2026).
29 Zhu, Y. *et al.* A 5-mm Untethered Crawling Robot via Self-Excited Electrostatic Vibration. *IEEE Trans. Rob.* **38**, 719-730 (2022).
30 Mao, G. *et al.* Ultrafast small-scale soft electromagnetic robots. *Nat. Commun.* **13**, 4456 (2022).
31 Xiong, Q., Zhou, X., Li, D., Ambrose, J. W. & Yeow, R. C.-H. An Amphibious Fully-Soft Centimeter-Scale Miniature Crawling Robot Powered by Electrohydraulic Fluid Kinetic Energy. *Adv. Sci.* **11**, 2308033, doi:https://doi.org/10.1002/advs.202308033 (2024).
32 Cheng, J. *et al.* Soft Crawling Microrobot Based on Flexible Optoelectronics Enabling Autonomous Phototaxis in Terrestrial and Aquatic Environments. *Soft Rob.* **12**, 45-55, doi:10.1089/soro.2023.0112 (2024).
33 Voise, J. & Casas, J. The management of fluid and wave resistances by whirligig beetles. *Journal of The Royal Society Interface* **7**, 343-352, doi:10.1098/rsif.2009.0210 (2009).
34 Liu, X. *et al.* Moving Mechanism of a High-speed Insect-scale Microrobot via Electromagnetically Induced Vibration. *J. Bionic Eng.* **18**, 662-673, doi:10.1007/s42235-021-0037-8 (2021).
35 Kinoshita, C., Fukuoka, T., Narazaki, T., Niizuma, Y. & Sato, K. Analysis of why sea turtles swim slowly: a metabolic and mechanical approach. *J. Exp. Biol.* **224**, jeb236216, doi:10.1242/jeb.236216 (2021).
36 Mazouchova, N., Gravish, N., Savu, A. & Goldman, D. I. Utilization of granular solidification during terrestrial locomotion of hatchling sea turtles. *Biol Lett* **6**, 398-401, doi:10.1098/rsbl.2009.1041 (2010).
37 Shine, R. & Shetty, S. Moving in two worlds: aquatic and terrestrial locomotion in sea snakes (Laticauda colubrina,

Laticaudidae). *J. Evol. Biol.* **14**, 338-346, doi:10.1046/j.1420-9101.2001.00265.x (2001).
38 Cheu, A. Y., Reed, S. A., Mann, S. D. & Bergmann, P. J. Performance and Kinematic Differences Between Terrestrial and Aquatic Running in Anolis Sagrei. *Integr. Comp. Biol.* **62**, 840-851, doi:10.1093/icb/icac031 (2022).
39 Freitas, G., Gleizer, G., Lizarralde, F., Hsu, L. & dos Reis, N. R. S. Kinematic reconfigurability control for an environmental mobile robot operating in the Amazon rain forest. *J. Field Rob.* **27**, 197-216, doi:https://doi.org/10.1002/rob.20334 (2010).
40 Kaznov, V. & Seeman, M. in *2010 IEEE/RSJ International Conference on Intelligent Robots and Systems.* 5113-5118.
41 Li, N., Ma, S., Wang, M., Li, B. & Wang, Y. in *2012 IEEE/RSJ International Conference on Intelligent Robots and Systems.* 2282-2288.
42 Crespi, A. & Ijspeert, A. J. Online Optimization of Swimming and Crawling in an Amphibious Snake Robot. *IEEE Trans. Rob.* **24**, 75-87, doi:10.1109/TRO.2008.915426 (2008).
43 Crespi, A., Lachat, D., Pasquier, A. & Ijspeert, A. J. Controlling swimming and crawling in a fish robot using a central pattern generator. *Autonomous Robots* **25**, 3-13, doi:10.1007/s10514-007-9071-6 (2008).
44 Yu, J. *et al.* On a Bio-inspired Amphibious Robot Capable of Multimodal Motion. *IEEE/ASME Trans. Mechatron.* **17**, 847-856, doi:10.1109/TMECH.2011.2132732 (2012).
45 Klein, M. A., Boxerbaum, A. S., Quinn, R. D., Harkins, R. & Vaidyanathan, R. in *2012 4th IEEE RAS & EMBS International Conference on Biomedical Robotics and Biomechatronics (BioRob).* 1335-1340.
46 Liang, X. *et al.* in *2012 IEEE/RSJ International Conference on Intelligent Robots and Systems.* 3667-3672.
47 Jin, H. *et al.* A starfish robot based on soft and smart modular structure (SMS) actuated by SMA wires. *Bioinspiration Biomimetics* **11**, 056012, doi:10.1088/1748-3190/11/5/056012 (2016).
48 Faudzi, A. A. M., Razif, M. R. M., Endo, G., Nabae, H. & Suzumori, K. in *2017 IEEE International Conference on Advanced Intelligent Mechatronics (AIM).* 981-986.
49 Zhu, P. *et al.* Light-Driven Amphibious Mini Soft Robot Mimicking the Locomotion Gait of Inchworm and Water Strider. *Advanced Intelligent Systems* **6**, 2300466, doi:https://doi.org/10.1002/aisy.202300466 (2024).
50 Li, Q., Zhang, F., Jing, Z., Yu, F. & Chen, Y. A Hybrid Territorial Aquatic Bionic Soft Robot with Controllable Transition Capability. *J. Bionic Eng.* **20**, 568-583, doi:10.1007/s42235-022-00294-x (2023).
51 Hwang, J. & Wang, W. D. Shape Memory Alloy-Based Soft Amphibious Robot Capable of Seal-Inspired Locomotion. *Advanced Materials Technologies* **7**, 2101153, doi:https://doi.org/10.1002/admt.202101153 (2022).
52 Milana, E. *et al.* in *2020 3rd IEEE International Conference on Soft Robotics (RoboSoft).* 766-771.
53 Tang, Y., Zhang, Q., Lin, G. & Yin, J. Switchable Adhesion Actuator for Amphibious Climbing Soft Robot. *Soft Rob.* **5**, 592-600, doi:10.1089/soro.2017.0133 (2018).
54 Cheng, Z. *et al.* A Highly Robust Amphibious Soft Robot with Imperceptibility Based on a Water-Stable and Self-Healing Ionic Conductor. *Adv. Mater.* **35**, 2301005, doi:https://doi.org/10.1002/adma.202301005 (2023).
55 Goldberg, B. *et al.* Power and Control Autonomy for High-Speed Locomotion With an Insect-Scale Legged Robot. *IEEE Rob. Autom. Lett.* **3**, 987-993, doi:10.1109/LRA.2018.2793355 (2018).
56 Wood, R. J., Avadhanula, S., Sahai, R., Steltz, E. & Fearing, R. S. Microrobot Design Using Fiber Reinforced Composites. *J. Mech. Des.* **130** (2008).

Acknowledgments

This work is supported by the National Key Research and Development Program of China (Grant No. 2024YFB4710500), AECC Industry-university Collocation Fund under Grant HFZL2023CXY026, National Natural Science Foundation of China (Grant No. 62503026 and No. 524B2057). Any opinions, findings, conclusions, or recommendations expressed in this material are those of the authors and do not necessarily

reflect the views of the National Natural Science Foundation of China.

Author contribution

Zhiwei Liu and Wencheng Zhan proposed and designed the research. Wencheng Zhan, Xiaoxi Li, Zhiwei Liu and Delan Huang designed and built the microrobot. Wencheng Zhan, Xiaoxi Li, Zhiwei Liu, Delan Huang, Xian Yu, Zhaoli Wei, Jiaming Leng, Heming Xu, Chunxiao Li and Pei Cai conducted the experimental work. Wencheng Zhan, Xiaoxi Li, Zhiwei Liu, Jia Hu, Xian Yu, and Zhaoli Wei contributed to the dynamic modeling and data analysis. Wencheng Zhan and Xiaoxi Li drafted the manuscript. Zhiwei Liu and Xiaojun Yan revised the manuscript. All authors provided feedback.

Competing interests

The authors declare no competing interests.

Inclusion & Ethics

This work is achieved by researchers from Beihang University. All the relevant researchers fulfilling the authorship criteria are included as the co-authors. The supported foundations are also listed in the Acknowledgements section. In addition, this work is in compliance with the general policies on Research ethics of Nature Communications.

Supplementary Information

Asymmetric vibration pattern enables ultrafast locomotion of an insect-scale amphibious microrobot

Supplementary Information contains:

Supplementary Notes 1-2
Supplementary Figures 1-7
Supplementary Tables 1-3
Supplementary References
Captions of Supplementary Movies 1-12

Supplementary Notes 1-2

S1. Dynamical model of the microrobot under aquatic locomotion mode

A simplified dynamic model is developed to investigate the locomotion characteristics of the microrobot on the water surface, which consists of two rigid bodies M_f (relatively stationary parts including support frames, buoyancy tank, and rear legs) and M_{pd} (swimming paddles), a lumped mass m_e (equivalent of the permanent magnet and the simply supported beams within the electromagnetic actuator), as shown in Fig. 2d. Several simplifications are adopted to highlight the governing influence of design parameters of the swimming paddle:

(1) The actuation mechanism engages with the water surface via two components: the front legs and the swimming paddles. When the microrobot floats on the water surface, the front legs are oriented perpendicular to the water surface. Their swinging motion is theoretically symmetric, yielding zero net propulsive force. Therefore, the front legs are excluded from the dynamic model of the microrobot, with only the swimming paddles taken into account.

(2) The output parameters of the two electromagnetic actuators are the same. Therefore, two swimming paddles connected with two actuators respectively are simplified to one rigid body M_{pd}.

(3) The unidirectional passive hinge of the swimming paddle is simplified as a torsional spring (k_θ) exhibiting asymmetric elastic and damping coefficients between clockwise and counterclockwise rotations.

(4) On the water surface, the vertical degree of freedom of the microrobot was omitted in favor of its forward degree of freedom.

We utilize the Lagrangian method to establish the dynamical equations of the microrobot. Three generalized coordinates q_i (i = 1, 2, 3) are selected to characterize the locomotion of the microrobot: x, s, and θ_s. x is the lateral displacement along the x-axis for the COM of M_f in the inertial coordinate system (x-o-y). s is the

relative displacement of m_e with respect to M_f along the *x*-axis. θ_s is the swing angle of M_{pd} relative to M_f. The Lagrange function can be given as:

$$\frac{d}{dt}\frac{\partial L}{\partial \dot{q}_i}-\frac{\partial L}{\partial q_i}=Q_i \tag{1}$$

$$\begin{bmatrix} 2m+M+2m_{pd} & 2m-2m_{pd}T & m_{pd}h_{pd}\cos\theta_s \\ 2m-2m_{pd}T & 2m+2m_{pd}T^2 & -m_{pd}h_{pd}T\cos\theta_s \\ m_{pd}h_{pd}\cos\theta_s & -m_{pd}h_{pd}T\cos\theta_s & 0.5m_{pd}h_{pd}^2+2J_{pd} \end{bmatrix}\begin{bmatrix} \ddot{x} \\ \ddot{s} \\ \ddot{\theta}_s \end{bmatrix}=\begin{bmatrix} m_{pd}h_{pd}\dot{\theta}_s^2\sin\theta_s+F_1 \\ -m_{pd}Th_{pd}\dot{\theta}_s^2\sin\theta_s-2ks+F_2 \\ k_\theta\theta_s+F_3 \end{bmatrix} \tag{2}$$

where m, M and m_{pd} are the masses of m_e, M_f and M_{pd}; T is the displacement transmission ratio from the actuator-connected end to the paddle-attached end of the simply supported beams; J_{pd} is the moment of inertia of M_{pd}; h_{pd} is the height of M_{pd}; k is the elastic coefficient of the simply supported beams; k_θ is the torsional elastic coefficient of the passive hinge of the swimming paddle; F_1, F_2, and F_3 are the generalized forces associated with three generalized coordinates. Their explicit expressions are:

$$\begin{bmatrix} F_1 \\ F_2 \\ F_3 \end{bmatrix}=\begin{bmatrix} F_{af}+F_{wf}+F_{pd} \\ F_{EM}+F_{am}-TF_{pd} \\ T_{pd} \end{bmatrix} \tag{3}$$

where F_{af} and F_{wf} are the air and water damping forces applying on rigid body M_f respectively; F_{pd} and T_{pd} are the water damping force and torque applying on rigid body M_{pd} respectively; F_{EM} is the electromagnetic force applying on the lumped mass m_e; F_{am} is the air damping force applying on the lumped mass m_e.

The three damping forces, F_{af}, F_{am}, and F_{wf}, in Eq. (3) exhibit similar functional form:

$$\begin{cases} F_{af}=-0.5C_aA_{af}\rho_{air}\dot{x}^2\,\mathrm{sgn}(\dot{x}) \\ F_{am}=-0.5C_aA_m\rho_{air}\dot{x}_m^2\,\mathrm{sgn}(\dot{x}_m) \\ F_{wf}=-0.5C_{w1}A_{wf}\rho_{water}\dot{x}^2\,\mathrm{sgn}(\dot{x}) \end{cases} \tag{4}$$

where C_a is the air damping coefficient; ρ_{air} is the density of air; A_{af} is the cross-sectional area of the portion of the body M_f exposed to the air, perpendicular to the *x-axis*; A_m is the area of the surface perpendicular to the *x-axis* for the lumped mass m_e; C_{w1} is the water damping coefficient of the body M_f; ρ_{water} is the density of water; A_{wf} is the cross-sectional area of the submerged portion of the body M_f, perpendicular to the *x-axis*.

The electromagnetic force F_{EM} depends on the input current signal and the structural parameters of the electromagnetic actuator, and can be specifically expressed as:

$$F_{EM}=\frac{B_r(B_{z1}-B_{z2})A}{\mu_0}=\frac{\pi B_r(B_{z1}-B_{z2})R^2}{\mu_0} \tag{5}$$

where B_r is the residual magnetization of the magnet; B_{z1} is the magnetic field strength of the lower surface of the magnet in the axial direction; B_{z2} is the magnetic field strength of the upper surface of the magnet in the axial direction; R is the radius of the magnet; μ_0 is the permeability of vacuum. B_{z1} and B_{z2} are:

$$\begin{cases} B_{z1}=B_z(z)=\dfrac{\mu_0 NI}{2}\left(\dfrac{l-z}{\sqrt{(l-z)^2+r^2}}+\dfrac{z}{\sqrt{z^2+r^2}}\right) \\ B_{z2}=B_z(z+L)=\dfrac{\mu_0 NI}{2}\left(-\dfrac{z+L-l}{\sqrt{(z+L-l)^2+r^2}}+\dfrac{z+L}{\sqrt{(z+L)^2+r^2}}\right) \end{cases} \tag{6}$$

where z is the distance from the lower surface of the magnet to the lower surface of the coil; N is the number of turns of the coil; I is the current flowing through the coil; l is the axial length of the coil; r is the radius of the coil; L is the axial length of the magnet.

As the paddle undergoes compound rigid-body motion involving both translation and rotation, the resultant force F_{pd} and moment T_{pd} exerted on it in Equation (3) should be computed via integration:

$$\begin{cases} F_{pd}=\dfrac{1}{2}\rho_{water}C_{w2}w_{pd}\displaystyle\int_{-h_{pd}}^{0} v_{pd,n}^2\,\mathrm{sgn}\left(-v_{pd,n}\right)dy_{pd} \\ T_{pd}=\dfrac{1}{2}\rho_{water}C_{w2}w_{pd}\displaystyle\int_{-h_{pd}}^{0} -v_{pd,n}^2 y_{pd}\,\mathrm{sgn}\left(-v_{pd,n}\right)dy_{pd} \end{cases} \tag{7}$$

where C_{w2} is the water damping coefficient of the body M_{pd}; w_{pd} and h_{pd} are the width and height of the swimming paddle respectively; $v_{pd,n}$ is the surface-normal velocity of a point on the paddle in the inertial coordinate system.

S2. Dynamical model of the microrobot under terrestrial locomotion mode

In order to analyze the terrestrial locomotion characteristics of the microrobot, a separate dynamic model is also established. Similar to the dynamic model for aquatic locomotion, the microrobot is simplified as a

dynamic system composed of a rigid body M_b and a lumped mass m_e, as shown in Supplementary Fig. 5. Three simplifications are introduced to this model:

(1) The output parameters of the two electromagnetic actuators are the same. Therefore, two front legs connecting with two actuators respectively are simplified to one front leg.

(2) The simply supported beams are simplified as a massless spring with an elastic coefficient of k.

(3) The magnet is simplified as a lumped mass m_e, and the remaining components of the microrobot form the rigid body M_b, including the supporting frames, coil and legs.

(4) The action between the feet of the microrobot and the ground is simplified as a vertical spring-damper (k_y-d_y) with a normal force in the vertical direction (F_N) and a friction force in the lateral direction (F_f). Several key geometric dimensions of the microrobot are illustrated in Supplementary Fig. 5.

Two coordinate systems are developed to characterize the motion of the microrobot, including the inertial coordinate system x-o-y and the body coordinate system x'-o-y' with the center of mass (COM) of rigid body M_b as the origin, as shown in Supplementary Fig. 5. The Lagrangian method is used to establish the dynamic equations of the microrobot based on four generalized coordinates, including the horizontal and vertical coordinates (x, y) of the COM of the rigid body M_b, the displacement s of the lumped mass m_e relative to its initial position in the body direction, and the body tilt angle θ_b. The absolute coordinates of any point (x_p, y_p) in the system can be obtained through these generalized coordinates and the transform relation between two coordinate systems:

$$\begin{pmatrix} x_p \\ y_p \end{pmatrix} = \begin{pmatrix} \cos\theta_b & -\sin\theta_b \\ \sin\theta_b & \cos\theta_b \end{pmatrix} \begin{pmatrix} x' \\ y' \end{pmatrix} + \begin{pmatrix} x \\ y \end{pmatrix} \tag{8}$$

The lagrangian equations of the dynamic model can be given as:

$$\frac{d}{dt}\left(\frac{\partial L}{\partial \dot{q}_i}\right) - \frac{\partial L}{\partial q_i} = Q_i \quad (i=1,2,3,4) \tag{9}$$

$$\begin{bmatrix} 2m+M & 0 & 2m\cos\theta_b & A \\ 0 & 2m+M & 2m\sin\theta_b & B \\ 2m\cos\theta_b & m\sin\theta_b & m & -2ml_m \\ A & B & -2ml_m & C \end{bmatrix}\begin{bmatrix} \ddot{x} \\ \ddot{y} \\ \ddot{s} \\ \ddot{\theta}_b \end{bmatrix}=\begin{bmatrix} 2m\dot{s}\dot{\theta}_b\sin\theta_b+m(r_m+s)\dot{\theta}_b^2\cos\theta_b+F_1 \\ -2m\dot{s}\dot{\theta}_b\cos\theta_b+m(r_m+s)\dot{\theta}_b^2\sin\theta_b-(m+M)g+F_2 \\ m\dot{x}\dot{\theta}_b\sin\theta_b-m\dot{y}\dot{\theta}_b\cos\theta_b-ks+F_3 \\ -2m(r_m+s)\dot{s}\dot{\theta}_b-mg(r_m+s)\cos\theta_b+F_4 \end{bmatrix} \tag{10}$$

$$\begin{cases} A=-2m\left(r_m+s\right)\sin\theta_b-2ml_m\cos\theta_b \\ B=2m\left(r_m+s\right)\cos\theta_b-2ml_m\sin\theta_b \\ C=2m\left(r_m+s\right)^2+2ml_m^2+J_b \end{cases} \tag{11}$$

where m and M are the masses of the lumped mass m_e and rigid body M_b; r_m is the relative distance between m_e (at the initial position) and the COM of M_b along x'-axis; k is the elastic coefficient of the simply supported beams; l_m is the relative distance between m (at the initial position) and the COM of M_b along y'-axis; J_b is the moments of inertia of M_b; h_b is the height of M_b; F_1, F_2, F_3 and F_4 are the generalized forces associated with four generalized coordinates. Their explicit expressions are:

$$\begin{bmatrix} F_1 \\ F_2 \\ F_3 \\ F_4 \end{bmatrix}=\begin{bmatrix} 2F_{fr}+2F_{ff}+F_{dx,b} \\ 2F_{Nr}+2F_{Nf}+F_{dy,b} \\ F_{EM}+F_{dm}+2F_{ff}\left(-T\cos\theta_b\right)+2F_{ff}\left(-T\sin\theta_b\right) \\ 2T_{fr}+2T_{ff}+T_d \end{bmatrix} \tag{12}$$

where F_{fr} and F_{ff} are the frictional forces applying on the rear and front legs respectively; F_{Nr} and F_{Nf} are the normal forces applying on the rear and front legs respectively; $F_{dx,\,b}$ and $F_{dy,\,b}$ are the air damping forces applying on the rigid body M_b in the x-axis and y-axis direction respectively; F_{dm} is the air damping forces applying on the lumped mass m_e in the x'-axis direction; F_{EM} is the electromagnetic force applying on the lumped mass m_e; T is the displacement transmission ratio from the actuator-connected end to the paddle-attached end of the simply supported beams; T_{fr} and T_{ff} are the friction torques applying on the rear and front legs respectively; T_d is the damping torque from air applying on the rigid body M_b.

Based on the spring-damper model between the feet and the ground, the normal forces are given as (13) and (14) when the feet are in contact with the ground. If one foot is off the ground, the corresponding normal force and frictional force are both equal to zero.

$$\begin{cases} F_{Nr}=\mathrm{sgn}(-y_{fr})\times(-k_y y_{fr}-d_y\dot{y}_{fr}) \\ F_{Nf}=\mathrm{sgn}(-y_{ff})\times(-k_y y_{ff}-d_y\dot{y}_{ff}) \end{cases} \tag{13}$$

$$\begin{cases} F_{\mathrm{fr}} = \mathrm{sgn}(-\dot{x}_{\mathrm{fr}})\mu F_{\mathrm{Nr}} \\ F_{\mathrm{ff}} = \mathrm{sgn}(-\dot{x}_{\mathrm{ff}})\mu F_{\mathrm{Nf}} \end{cases} \tag{14}$$

where x_{fr}, y_{fr} are the coordinates of the rear foot in the inertial coordinate system; x_{ff}, y_{ff} are the coordinates of the front foot in the inertial coordinate system; k_y, d_y are the elastic coefficient and damping coefficient respectively when the feet are in contact with the ground; μ is the friction coefficient between the feet and ground.

The air damping forces in (12) are expressed as:

$$\begin{cases} F_{\mathrm{dx,\,b}} = -0.5 C_{\mathrm{a}} A_{\mathrm{bx}} \rho_{\mathrm{air}} \dot{x}^2 \,\mathrm{sgn}(\dot{x}) \\ F_{\mathrm{dy,\,b}} = -0.5 C_{\mathrm{a}} A_{\mathrm{by}} \rho_{\mathrm{air}} \dot{y}^2 \,\mathrm{sgn}(\dot{y}) \\ F_{\mathrm{dm}} = -0.5 C_{\mathrm{a}} A_{\mathrm{m}} \rho_{\mathrm{air}} \dot{x}_{\mathrm{m}}^2 \,\mathrm{sgn}(\dot{x}_{\mathrm{m}}) \end{cases} \tag{15}$$

where C_{a} is the air damping coefficient; ρ_{air} is the density of air; A_{bx} is the area of the surface perpendicular to the *x-axis* for the body $\mathrm{M_b}$; A_{by} is the area of the surface perpendicular to the *y-axis* for the body $\mathrm{M_b}$; A_{m} is the area of the surface perpendicular to the *x-axis* for the lumped mass $\mathrm{m_e}$.

The torques in (12) are expressed as:

$$\begin{cases} T_{\mathrm{fr}} = F_{\mathrm{fr}}(r_{\mathrm{fr}} \sin\theta_{\mathrm{b}} + l_{\mathrm{fr}} \cos\theta_{\mathrm{b}}) - F_{\mathrm{Nr}}(r_{\mathrm{fr}} \cos\theta_{\mathrm{b}} - l_{\mathrm{fr}} \sin\theta_{\mathrm{b}}) \\ T_{\mathrm{ff}} = F_{\mathrm{ff}}(r_{\mathrm{ff}} \cos\theta_{\mathrm{b}} - l_{\mathrm{ff}} \sin\theta_{\mathrm{b}}) + F_{\mathrm{Nf}}(r_{\mathrm{ff}} \sin\theta_{\mathrm{b}} + l_{\mathrm{ff}} \cos\theta_{\mathrm{b}}) \\ T_{\mathrm{d}} = -0.5 C_{\mathrm{a}} \rho_{\mathrm{air}} \int_{-x_{\mathrm{r}}}^{x_{\mathrm{f}}} \left(x\dot{\theta}_{\mathrm{b}}\right)^2 w(x) \,\mathrm{sgn}\left(\dot{\theta}_{\mathrm{b}}\right) dx \end{cases} \tag{16}$$

where r_{fr} is the distance between the rear feet and the COM of $\mathrm{M_b}$ along x'-axis; l_{fr} *is* the distance between the rear feet and the COM of $\mathrm{M_b}$ along y'-axis; r_{ff} is the distance between the front feet and the COM of $\mathrm{M_b}$ along x'-axis; l_{ff} *is* the distance between the front feet and the COM of $\mathrm{M_b}$ along y'-axis; x_{f} is the distance between the COM of $\mathrm{M_b}$ and the front end along x'-axis; x_{r} is the distance between the COM of $\mathrm{M_b}$ and the rear end along x'-axis; $w(x)$ is the width function of $\mathrm{M_b}$ with elliptical shape.

1 Kinoshita, C., Fukuoka, T., Narazaki, T., Niizuma, Y. & Sato, K. Analysis of why sea turtles swim slowly: a metabolic and mechanical approach. *J. Exp. Biol.* **224**, jeb236216, doi:10.1242/jeb.236216 (2021).

2 Mazouchova, N., Gravish, N., Savu, A. & Goldman, D. I. Utilization of granular solidification during terrestrial locomotion of hatchling sea turtles. *Biol Lett* **6**, 398-401, doi:10.1098/rsbl.2009.1041 (2010).

3 Shine, R. & Shetty, S. Moving in two worlds: aquatic and terrestrial locomotion in sea snakes (Laticauda colubrina, Laticaudidae). *J. Evol. Biol.* **14**, 338-346, doi:10.1046/j.1420-9101.2001.00265.x (2001).

4 Cheu, A. Y., Reed, S. A., Mann, S. D. & Bergmann, P. J. Performance and Kinematic Differences Between Terrestrial and Aquatic Running in Anolis Sagrei. *Integr. Comp. Biol.* **62**, 840-851, doi:10.1093/icb/icac031 (2022).

5 Tang, L. *et al.* Inertia-driven amphibious robot with asymmetric microundulatory fin arrays. *Sci. Adv.* **12**, eaea2222, doi:10.1126/sciadv.aea2222 (2026).

6 Wang, D. *et al.* Miniature Amphibious Robot Actuated by Rigid-Flexible Hybrid Vibration Modules. *Adv. Sci.* **9**, 2203054, doi:https://doi.org/10.1002/advs.202203054 (2022).

7 Freitas, G., Gleizer, G., Lizarralde, F., Hsu, L. & dos Reis, N. R. S. Kinematic reconfigurability control for an environmental mobile robot operating in the Amazon rain forest. *J. Field Rob.* **27**, 197-216, doi:https://doi.org/10.1002/rob.20334 (2010).

8 Kaznov, V. & Seeman, M. in *2010 IEEE/RSJ International Conference on Intelligent Robots and Systems*. 5113-5118.

9 Li, N., Ma, S., Wang, M., Li, B. & Wang, Y. in *2012 IEEE/RSJ International Conference on Intelligent Robots and Systems*. 2282-2288.

10 Crespi, A. & Ijspeert, A. J. Online Optimization of Swimming and Crawling in an Amphibious Snake Robot. *IEEE Trans. Rob.* **24**, 75-87, doi:10.1109/TRO.2008.915426 (2008).

11 Crespi, A., Lachat, D., Pasquier, A. & Ijspeert, A. J. Controlling swimming and crawling in a fish robot using a central pattern generator. *Autonomous Robots* **25**, 3-13, doi:10.1007/s10514-007-9071-6 (2008).

12 Zhong, B. *et al.* On a CPG-Based Hexapod Robot: AmphiHex-II With Variable Stiffness Legs. *IEEE/ASME Trans. Mechatron.* **23**, 542-551, doi:10.1109/TMECH.2018.2800776 (2018).

13 Li, M., Guo, S., Hirata, H. & Ishihara, H. Design and performance evaluation of an amphibious spherical robot. *Rob. Auton. Syst.* **64**, 21-34, doi:https://doi.org/10.1016/j.robot.2014.11.007 (2015).

14 Yang, Y., Zhou, G., Zhang, J., Cheng, S. & Fu, M. in *2015 IEEE/RSJ International Conference on Intelligent Robots and Systems (IROS)*. 559-566.

15 Crespi, A., Karakasiliotis, K., Guignard, A. & Ijspeert, A. J. Salamandra Robotica II: An Amphibious Robot to Study Salamander-Like Swimming and Walking Gaits. *IEEE Trans. Rob.* **29**, 308-320, doi:10.1109/TRO.2012.2234311 (2013).

16 Yu, J. *et al.* On a Bio-inspired Amphibious Robot Capable of Multimodal Motion. *IEEE/ASME Trans. Mechatron.* **17**, 847-856, doi:10.1109/TMECH.2011.2132732 (2012).

17 Xing, H. *et al.* in *2019 IEEE/RSJ International Conference on Intelligent Robots and Systems (IROS)*. 1702-1707.

18 Klein, M. A., Boxerbaum, A. S., Quinn, R. D., Harkins, R. & Vaidyanathan, R. in *2012 4th IEEE RAS & EMBS International Conference on Biomedical Robotics and Biomechatronics (BioRob)*. 1335-1340.

19 Wang, G. *et al.* Subsea crab bounding gait of leg-paddle hybrid driven shoal crablike robot. *Mechatronics* **48**, 1-11, doi:https://doi.org/10.1016/j.mechatronics.2017.10.002 (2017).

20 Zhang, S. *et al.* AmphiHex-I: Locomotory Performance in Amphibious Environments With Specially Designed Transformable Flipper Legs. *IEEE/ASME Trans. Mechatron.* **21**, 1720-1731, doi:10.1109/TMECH.2015.2490074 (2016).

21 Liang, X. *et al.* in *2012 IEEE/RSJ International Conference on Intelligent Robots and Systems*. 3667-3672.

22 Jin, H. *et al.* A starfish robot based on soft and smart modular structure (SMS) actuated by SMA wires. *Bioinspiration Biomimetics* **11**, 056012, doi:10.1088/1748-3190/11/5/056012 (2016).

23 Faudzi, A. A. M., Razif, M. R. M., Endo, G., Nabae, H. & Suzumori, K. in *2017 IEEE International Conference on Advanced Intelligent Mechatronics (AIM)*. 981-986.

24 Chen, Y., Doshi, N., Goldberg, B., Wang, H. & Wood, R. J. Controllable water surface to underwater transition through electrowetting in a hybrid terrestrial-aquatic microrobot. *Nat. Commun.* **9**, 2495, doi:10.1038/s41467-018-04855-9 (2018).

25 Zhu, P. *et al.* Light-Driven Amphibious Mini Soft Robot Mimicking the Locomotion Gait of Inchworm and Water Strider. *Advanced Intelligent Systems* **6**, 2300466, doi:https://doi.org/10.1002/aisy.202300466 (2024).

26 Xiong, Q., Zhou, X., Li, D., Ambrose, J. W. & Yeow, R. C.-H. An Amphibious Fully-Soft Centimeter-Scale Miniature

Crawling Robot Powered by Electrohydraulic Fluid Kinetic Energy. *Adv. Sci.* **11**, 2308033, doi:https://doi.org/10.1002/advs.202308033 (2024).

27 Wu, G. *et al.* A piezoelectric driven amphibious microrobot capable of fast and controllable movement. *Smart Mater. Struct.* **33**, 115035, doi:10.1088/1361-665X/ad8610 (2024).

28 Cheng, J. *et al.* Soft Crawling Microrobot Based on Flexible Optoelectronics Enabling Autonomous Phototaxis in Terrestrial and Aquatic Environments. *Soft Rob.* **12**, 45-55, doi:10.1089/soro.2023.0112 (2024).

29 Li, Q., Zhang, F., Jing, Z., Yu, F. & Chen, Y. A Hybrid Territorial Aquatic Bionic Soft Robot with Controllable Transition Capability. *J. Bionic Eng.* **20**, 568-583, doi:10.1007/s42235-022-00294-x (2023).

30 Hwang, J. & Wang, W. D. Shape Memory Alloy-Based Soft Amphibious Robot Capable of Seal-Inspired Locomotion. *Advanced Materials Technologies* **7**, 2101153, doi:https://doi.org/10.1002/admt.202101153 (2022).

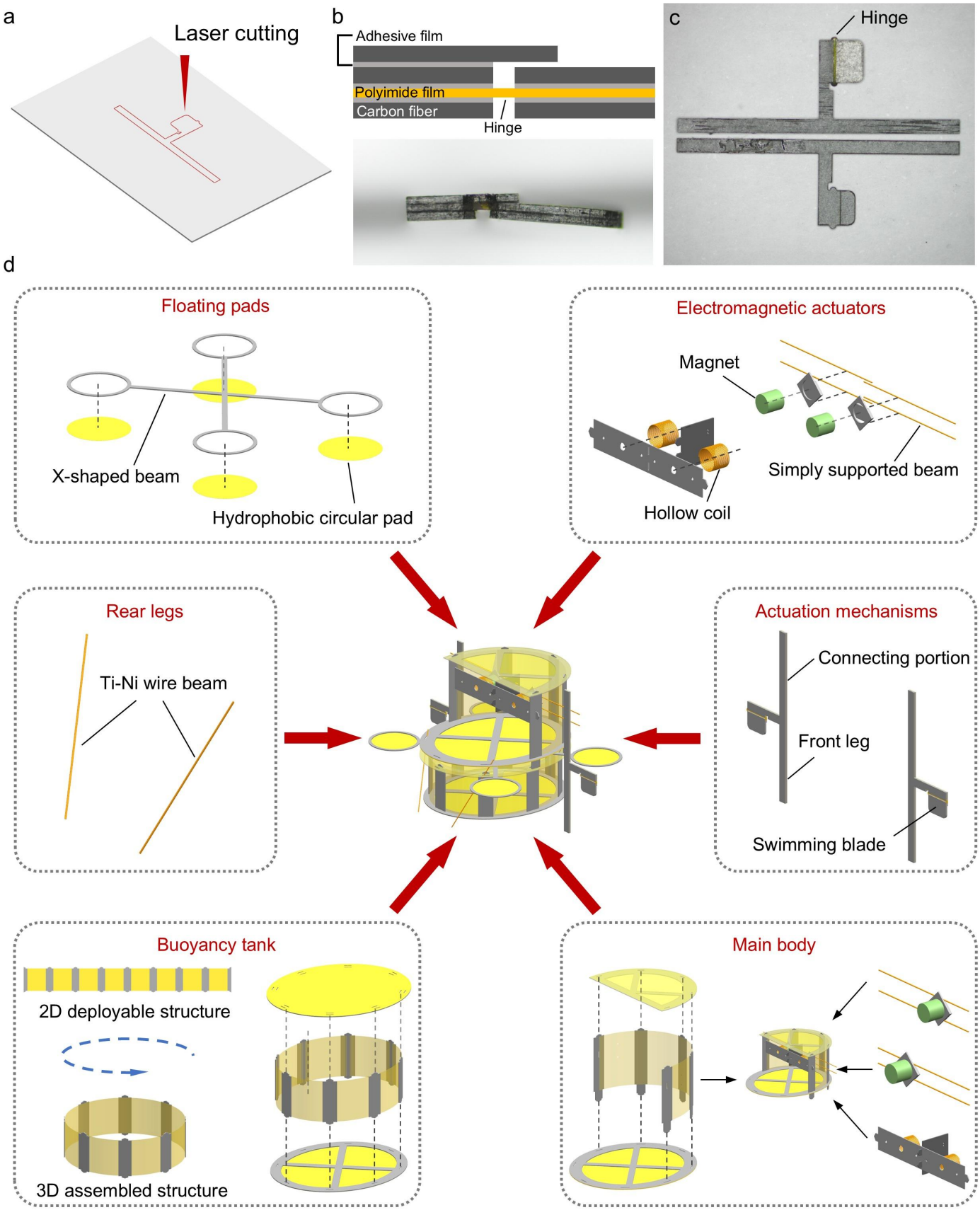
31 Milana, E. *et al.* in *2020 3rd IEEE International Conference on Soft Robotics (RoboSoft).* 766-771.

32 Tang, Y., Zhang, Q., Lin, G. & Yin, J. Switchable Adhesion Actuator for Amphibious Climbing Soft Robot. *Soft Rob.* **5**, 592-600, doi:10.1089/soro.2017.0133 (2018).

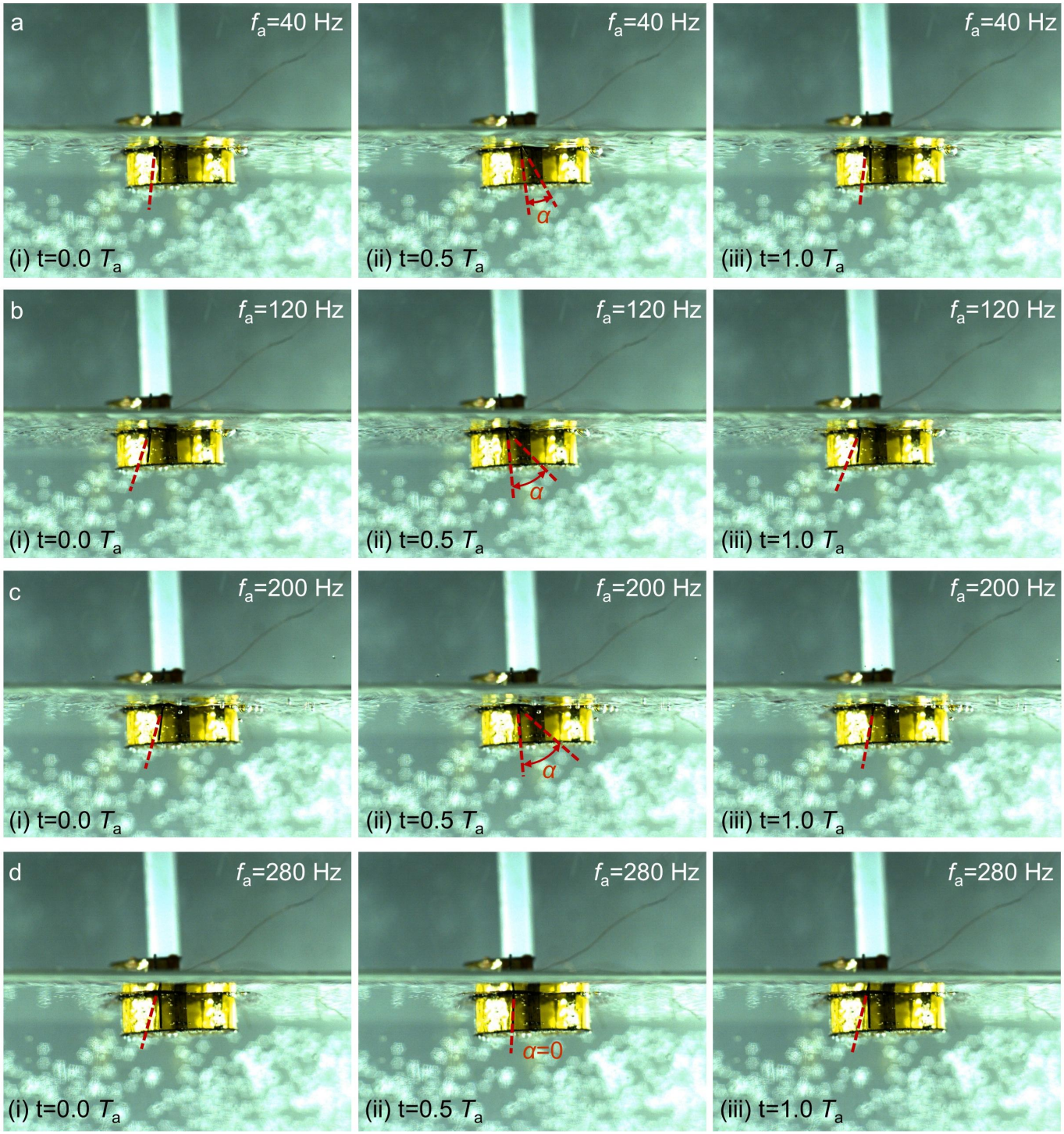
33 Wu, M. *et al.* A Fully 3D-Printed Tortoise-Inspired Soft Robot with Terrains-Adaptive and Amphibious Landing Capabilities. *Advanced Materials Technologies* **7**, 2200536, doi:https://doi.org/10.1002/admt.202200536 (2022).

34 Cheng, Z. *et al.* A Highly Robust Amphibious Soft Robot with Imperceptibility Based on a Water-Stable and Self-Healing Ionic Conductor. *Adv. Mater.* **35**, 2301005, doi:https://doi.org/10.1002/adma.202301005 (2023).

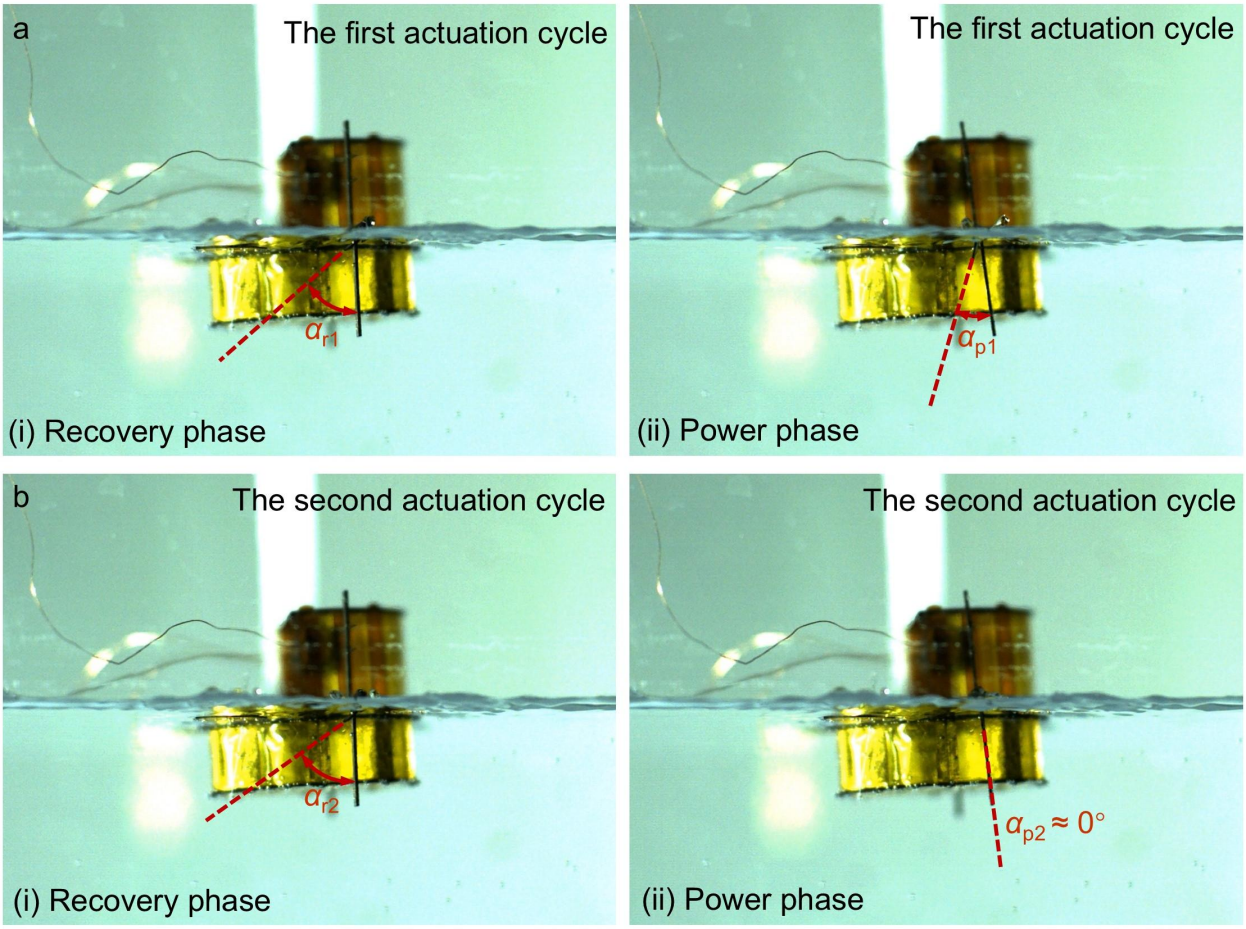
Supplementary Figures 1-7



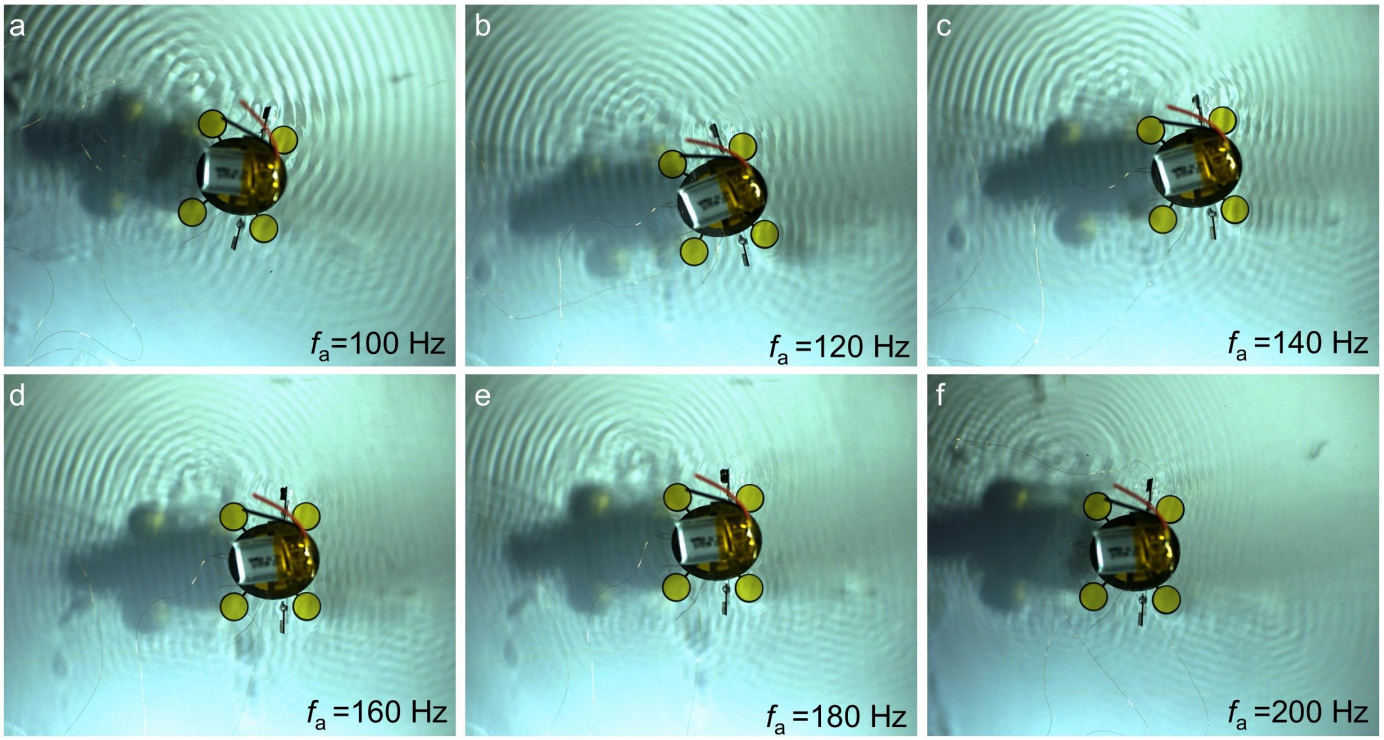
Supplementary Fig. 1. The fabrication process of the microrobot. a, Fabrication process of the swimming paddle via laser cutting. **b,** Diagram and optical photo showing the laminated structure of the swimming paddle. **c,** Optical photo of two swimming paddles with different dimensions. **d,** Manual assembly process of individual modules and the whole microrobot.



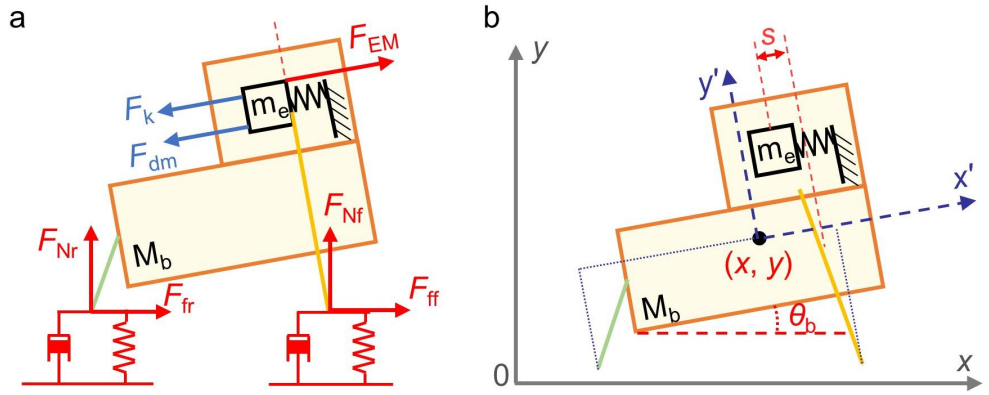
Supplementary Fig. 2. The swing motion of the swimming paddle under different actuating frequency f_a (40, 120, 200, and 280 Hz). As the actuation frequency approaches the natural frequency of the microrobot, the swing angle during recovery phase reaches its peak.



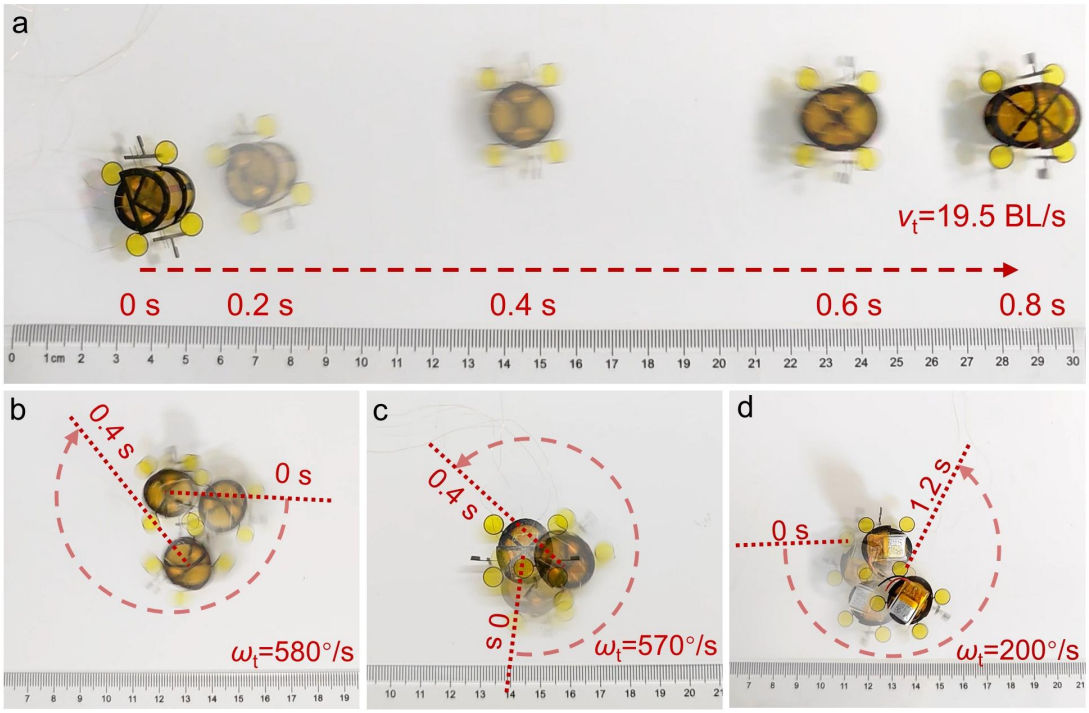
Supplementary Fig. 3. The swing motion of the swimming paddle under a small hinge thickness (4 μm). In every other actuation cycle, it is observed that the relative rotation angle of the swimming paddle α fails to return to 0° during the power phase.



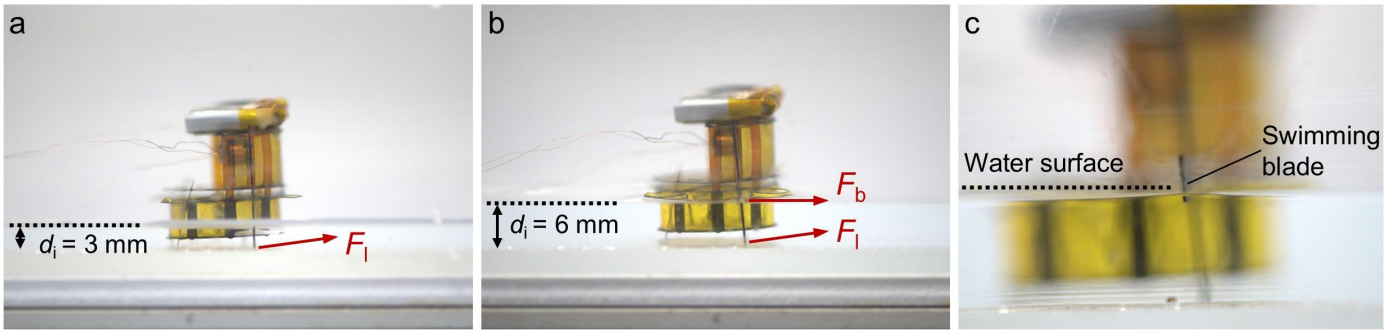
Supplementary Fig. 4. Propagation of water surface waves during the clockwise turning of the microrobot at different actuation frequencies (100, 120, 140, 160, 180, and 200 Hz).



Supplementary Fig. 5. Simplified dynamic model of the microrobot under terrestrial locomotion mode.



Supplementary Fig. 6. Tethered terrestrial locomotion performance of the microrobot on the plastic board. a, Optical photo of the tethered microrobot moving forward at a maximum speed of 19.5 BL/s on a plastic board without payload. **b, c,** Optical photos of the tethered microrobot achieving a maximum turning angular speed of 580°/s in the clockwise direction and 570°/s in the anticlockwise direction under a payload of 0 mg. **d,** Optical photo of the tethered microrobot achieving a maximum anticlockwise turning speed of 200°/s under a payload of 1200 mg.



Supplementary Fig. 7. Propulsion force analysis of the microrobot under varying immersion depths. a, At a 3 mm immersion depth, propulsion is generated exclusively by the front legs in contact with the ground. **b,** At a 6 mm immersion depth, propulsion is generated by both the front legs and the swimming paddles. **c,** Enlarged image of the paddle–water interface at a 6 mm immersion depth.

Supplementary Tables 1-3

Supplementary Table 1. The quantities and masses of individual components for the microrobot

Description	Quantity	Mass (mg)
Support frames	--	78
Simply supported beam	2	2
Permanent magnets	2	100
Hollow coils	2	102
Fixed boards for coils	1	13
Floating pads	4	29
Buoyancy tank	1	91
Front legs integrated with swimming paddles	2	30
Rear legs	2	1
Power and control electronics	1	555
Lithium battery	1	680
Wires and glue	--	≈ 9
Total		≈ 1690

Supplementary Table 2. Components of the power and control circuit board

Description	Model	Quantity	Weight (mg)
Microcontroller	RF-BM-4044B4	1	193.1
Voltage regulator (3.3V)	SPX3819M5	1	14.8
Voltage regulator (1.2V)	TLV75709PDBVR	1	15.2
Schmitt-Trigger inverter	SN74LVC2G14DCK	1	16.4
H-Bride driver	DRV8837C	2	19.6
Sensor (a microphone)	ICS-40181	1	60.0
Capacitor	0402; 0603	11	81.9
PCB	L: 17.5 mm; W:14.5 mm; Elliptical pattern	1	129.0
Solder	--	--	~25
Total weight			~555

Supplementary Table 3. Data of moving speed with respect to the body length of amphibians and existing amphibious robots

Species	Body length (cm)	Terrestrial relative speed (BL/s)	Aquatic relative speed (BL/s)	Reference
Amphibians				
Green turtle	≈50	≈0.4	≈1.0	[1,2]
Sea snakes (Laticauda colubrina)	≈80	≈0.3	≈1.4	[3]
Lizard (Anolis Sagrei)	≈5	≈11.0	≈7.0	[4]
Untethered amphibious robots				
Leglessbot	5.5	1.4	0.61	[5]
Robot by Zhao et al	7.5	10.90	2.30	[6]
EHR	73	3.15	1.23	[7]
Groundbot	60	5	--	[8]
Amoeba-II	65.51	--	0.21	[9]
Salamandra Robotica I	77	0.384	0.323	[10]
BoxyBot	25	--	1.4	[11]
AmphiHex-II	51.0	0.71	0.37	[12]
Spherical robot by Ishihara et al	25	0.9	0.644	[13]
FroBot	70	1.43	0.57	[14]
Salamandra Robotica II	110	0.38	0.46	[15]
AmphiRobot-II	70	0.86	0.64	[16]
ASRobot	30	0.18	0.12	[17]
SeaDog	114.5	2.0	--	[18]
Crablike robot by Xie et al	53.5	--	0.37	[19]
Tethered amphibious robots				
AmphiHex-I	84.4	0.65	0.59	[20,21]
Starfish robot	20	0.35	0.33	[22]
Soft-Amphibious Robot by Suzumori et al	21	0.27	0.105	[23]
HAMR	4.0	1.75	0.7	[24]
Mini-robot by Yang et al	2	0.05	0.5	[25]
MCR	5	0.32	--	[26]
SAM	4.5	3.4	2.02	[27]
Soft microrobot by Feng et al	3	0.13	--	[28]
Soft robot by Chen et al	9.5	1.79	0.316	[29]
SEALicone	25.74	--	0.07	[30]
EELWORM	40	0.033	0.05	[31]
ACSR	17.9	0.03	--	[32]
BASR	168	0.97	--	[33]
AISR	4.4	2.44	1.2	[34]
This work (untethered)				
This work	2.1	15.5	5.4	--

Captions of Supplementary Movie 1 to 12

Movie S1. Swing motion of the swimming paddle for the tethered microrobot during the swimming locomotion

This high-speed movie shows the swing motion of the swimming paddle for the tethered microrobot during the swimming locomotion. It is observed that the swimming paddle rotates around the hinge asymmetrically during the swimming locomotion.

Movie S2. Straight movements of the tethered microrobot on the water surface

This movie shows straight moving performance of two tethered microrobot prototypes (the original and the optimized) on the water surface when carrying a payload mass of 1200 mg. Part 1 shows the original prototype swimming forward with a relative speed of 3.7 BL/s. Part 2 shows the optimized prototype swimming forward with a relative speed of 5.5 BL/s.

Movie S3. Turns of the tethered microrobot on the water surface

This movie shows turning performance of the tethered microrobot on the water surface when carrying a payload mass of 1200 mg. Parts 1 and 2 show the microrobot achieving clockwise and anticlockwise turns on the water surface with a maximum turning speed of 370°/s and 280°/s respectively.

Movie S4. Untethered locomotion performance of the microrobot on the water surface

This movie shows untethered locomotion performance of the microrobot on the water surface when driven near its natural frequency. Part 1 shows the microrobot swimming linearly on the water surface with a maximum speed of 5.4 BL/s. Part 2 shows the microrobot achieving clockwise and anticlockwise turns on the water surface with a maximum turning speed of 450°/s and 360°/s respectively.

Movie S5. Obstacles avoidance via remote control on the water surface for the untethered microrobot

This movie shows the obstacle avoidance process of the untethered microrobot via navigating around immovable obstacles. The demonstration scenario is a 100 cm-by-60 cm water pool scattered with simulated

aquatic plants and lotus leaves. The microrobot traverses from the bottom-left corner to the top-right corner of the water pool, and subsequently navigates back to the bottom-left corner via an alternative route.

Movie S6. Pushing aside floating obstacles on water surface for the untethered microrobot

This movie shows the obstacle avoidance process of the untethered microrobot when encountering floating objects. During the process, the microrobot approaches, pushes away, and detaches from floating wooden blocks that are 6.6 times heavier than the microrobot itself.

Movie S7. Straight movements of the tethered microrobot on the ground

This movie shows straight moving performance of the tethered microrobot on the ground under different payload masses. Part 1 shows the microrobot moving forward at a maximum speed of 19.5 BL/s when carrying a payload of 0 mg. Part 2 shows the microrobot moving forward at a maximum speed of 11.9 BL/s when carrying a payload of 1200 mg.

Movie S8. Turns of the tethered microrobot on the ground

This movie shows turning performance of the tethered microrobot on the ground under different payload masses. Part 1 shows the microrobot achieving clockwise and anticlockwise turns on the ground with a maximum turning speed of 580°/s and 570°/s respectively when carrying a payload of 0 mg. Part 2 shows the microrobot achieving clockwise and anticlockwise turns on the ground with a maximum turning speed of 470°/s and 200°/s respectively when carrying a payload of 1200 mg.

Movie S9. Untethered locomotion performance of the microrobot on the ground

This movie shows the untethered locomotion performance of the microrobot on the ground when driven near its natural frequency. Part 1 shows the untethered microrobot running linearly on the plastic board with a maximum speed of 15.5 BL/s. Part 2 shows the untethered microrobot achieving clockwise and anticlockwise turns on a plastic board with a maximum turning speed of 760°/s and 470°/s respectively.

Movie S10. Slope climbing of the untethered microrobot

This movie shows the untethered microrobot crawling on a slope of 4° via a bipedal alternating relay climbing strategy within 30 s.

Movie S11. Water-traversing locomotion of the tethered microrobot

This movie shows the water traversing locomotion of the tethered microrobot at a submersion depth of 8 mm. The microrobot moves forward at a maximum speed of 5.4 BL/s, with the front leg and swimming paddle jointly generating propulsion.

Movie S12. Bidirectional transitions between the water surface and ground of the untethered microrobot via a slope

This movie shows that the untethered microrobot achieves bidirectional transitions between the water surface and ground via a slope. Part 1 shows the side view of the microrobot traversing the water surface, transitioning onto land via a slope, reversing direction, and returning to the water surface. Part 2 shows the top view of the whole process.

Supplementary Files

This is a list of supplementary files associated with this preprint. Click to download.

- SupplementaryMovie8.mp4
- SupplementaryInformation.pdf
- SupplementaryMovie7.mp4
- SupplementaryMovie4.mp4
- SupplementaryMovie1.mp4
- SupplementaryMovie12.mp4
- SupplementaryMovie2.mp4
- SupplementaryMovie10.mp4
- SupplementaryMovie11.mp4
- SupplementaryMovie9.mp4
- SupplementaryMovie5.mp4
- SupplementaryMovie6.mp4
- SupplementaryMovie3.mp4